J Intell Robot Syst
DOI 10.1007/s10846-013-9928-1

Efficient Flight Control via Mechanical Impedance Manipulation: Energy Analyses for Hummingbird-Inspired MAVs

Hosein Mahjoubi · Katie Byl

Received: 31 August 2013 / Accepted: 12 September 2013

Abstract Within the growing family of unmanned aerial vehicles (UAV), flapping-wing micro aerial vehicles (MAV) are a relatively new field of research. Inspired by small size and agile flight of insects and birds, these systems offer a great potential for applications such as reconnaissance, surveillance, search and rescue, mapping, etc. Nevertheless, practicality of these vehicles depends on how we address various challenges ranging from control methodology to morphological construction and power supply design. A reasonable approach to resolving such problems is to acquire further inspiration from solutions in nature. Through modeling synchronous muscles in insects, we have shown that manipulation of mechanical impedance properties at wing joints can be a very efficient method for controlling lift and thrust production in flapping-wing MAVs. In the present work, we describe how this approach can be used to decouple lift/thrust regulation, thus reducing the complexity of flight controller. Although of simple design, this controller is still capable of demonstrating a high degree of precision and maneuverability throughout various simulated flight experiments with different types of trajectories. Furthermore, we use these flight simulations to investigate the power requirements of our control approach. The results indicate that these characteristics are considerably lower compared to when conventional control strategies—methods that often rely on manipulating stroke properties such as frequency or magnitude of the flapping motion—are employed. With less power demands, we believe our proposed control strategy is able to significantly improve flight time in future flapping-wing MAVs.

Keywords Bio-inspired MAV · Flapping flight · Tunable impedance · Variable stiffness actuator · Maneuverability · Energy efficiency

1 Introduction

Originally introduced during World War I [1], Unmanned Aerial Vehicles (UAVs) have experienced a substantial level of growth over the past century; both in military and civilian application domains. Surveillance, reconnaissance, search and rescue, traffic monitoring, fire detection and environment mapping are just a few examples of their many possible applications.

H. Mahjoubi (✉) · K. Byl
Robotics Laboratory, Department of Electrical and Computer Engineering, University of California at Santa Barbara, Santa Barbara, CA 93106, USA
e-mail: h.mahjoubi@ece.ucsb.edu

K. Byl
e-mail: katiebyl@ece.ucsb.edu

Published online: 05 October 2013

UAVs can be categorized into three general groups: fixed-wing airplanes, rotary-wing vehicles and flapping wing systems. Each type has different advantages and disadvantages. However, as we go smaller in size to design Micro Aerial Vehicles (MAVs), the limitations of fixed and rotary-wing technologies become more apparent; the Reynolds number decreases as the wing surface becomes smaller, resulting in unsteady aerodynamic effects that are still a subject of research. On the other hand, flapping wing designs inspired by birds and insects offer the most potential for high maneuverability at miniaturized scales. Unparalleled dynamics, speed and agility are known traits of insects and hummingbirds that turn them into the most efficient flyers in nature. Furthermore, their ability to adapt with varying weather and environmental conditions is phenomenal; hence mimicking their flight dynamics [2–7] and actuation mechanisms would be a reasonable approach to designing practical MAVs. Note that in contrast to most birds whose wing stroke is largely restricted within the coronal plane, insects—and hummingbirds—employ a wing stroke motion that is mostly contained within the axial plane [5]. This feature enables the creature to control its thrust force and perform tasks such as hovering. A schematic description of wing stroke motion in insect flapping flight has been demonstrated in Fig. 1 [8].

Past research on flapping-wing MAVs has mainly concentrated on development of flapping mechanisms that are capable of producing sufficient lift for levitation. With such platforms available, e.g. *Harvard's Robotic Fly* [9], *Delfly* [10] and the *Entomopter* [11], force manipulation and motion control are the next challenges that must be faced. Recent work focused on vertical acceleration and altitude control has led to some impressive results [12, 13]. Research on forward flight control has been less developed in comparison [14]. In addition to flight control challenges, the small size of flapping-wing MAVs poses considerable limits on available space for actuators, power supplies and any sensory or control modules. Although a major portion of the overall mass is often allocated to batteries [9, 10], the flight time of these vehicles rarely exceeds a few minutes. Thus in terms of efficiency and flight duration, current flapping-wing MAVs are still far inferior to their fixed and rotary-wing counterparts.

The majority of works concentrating on force control employ modifications in wing-beat profile to achieve their objective [15, 16]. While this approach proves to be successful in separate control of lift [17] or horizontal thrust [18], simultaneous control of these forces is more challenging. Both forces are directly influenced by velocity of air flow over the wings, a factor that is heavily determined by the rate of wing-beat [19]. Therefore, modifying wing-beat profile will lead to coupling between lift and thrust forces, i.e. an inconvenience for motion control and maneuverability of the vehicle.

In contrast to stroke actuation methods, one could investigate possible mechanisms that insects and small birds employ to regulate aerodynamic force during various aerial maneuvers. Control strategies developed based on such mechanisms may further improve controllability and energy efficiency of future MAV prototypes. The *Tunable Impedance* (TI) method [20] is one such strategy. Inspired by the structure of antagonistic muscle pairs attached to wing joints—also known as synchronous muscles [21]—in insects

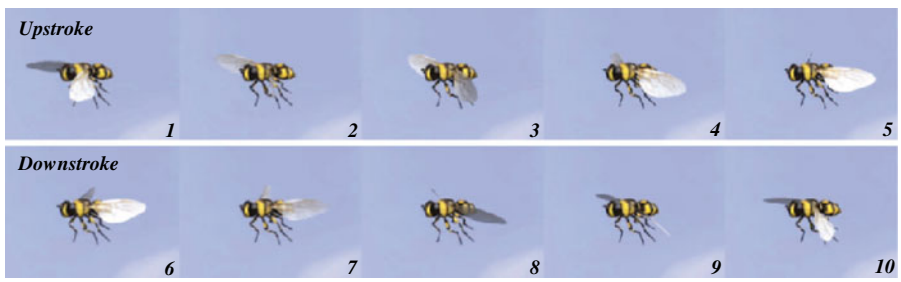

Fig. 1 Wing stroke cycle in insect flapping flight (adapted from [8])

and hummingbirds, we have previously shown that mechanical impedance properties of each wing joint can be modeled as a linear torsional spring [22, 23]. Tunable Impedance approach states that through manipulating the properties of these springs, one can modify the passive pitch reversal of each wing. Wing pitch reversal [24] plays a significant role in production and manipulation of lift/thrust through regulating the angle of attack (AoA) of the wing relative to air flow [19]. Thus, TI method can indirectly adjust the mean production of lift and thrust in each individual wing [20, 25]. Although this approach is able to provide a higher degree of controllability compared to traditional wing-beat modification approaches [25, 26], its lift and thrust manipulation procedures are not always completely decoupled [26].

In this work, our first goal is to identify the conditions that may reduce coupling between lift and thrust manipulation when TI approach is employed. We then use these findings to develop a motion controller that is capable of tracking various trajectories in the sagittal plane with a considerably high degree of precision as verified by our simulated experiments.

Unlike conventional approaches to flapping-wing MAV control, TI does not require any modifications in flapping properties such as frequency or magnitude of the stroke. This suggests that a fixed stroke profile can be used during all operational modes including takeoff, forward acceleration and hovering. Hence, regardless of the maneuver, the MAV will need a relatively constant amount of power to flap its wings. Naturally, this amount should be large enough to provide sufficient lift for levitation. Depending on the desired maneuver, extra power may be required to change the mechanical impedance properties of each wing joint via suitable actuators. Through simulated flight experiments, this work will show that such changes are often very small and do not demand considerable amounts of power. Thus, with a motion controller based on Tunable Impedance approach, we expect that an actual MAV's power requirements during any maneuver remain almost constant, i.e. close to the amount necessary for hovering. To appreciate the significance of this feature, a new set of flight experiments were simulated. In this group of experiments, wings' mechanical impedance properties were fixed and aerodynamic forces were controlled through changes in shape and frequency of the flapping profile. Comparing both cases, it is observed that power requirements in the Tunable Impedance method are considerably lower. Therefore, implementation of a similar control approach on an actual MAV may significantly improve efficiency and result in longer flight times.

The remainder of this work is organized as follows. Section 2 briefly explains our model for mechanical impedance at the wing joints. Section 3 reviews the employed aerodynamic model for flight simulations. Using this model, we will then describe the underlying concept of Tunable Impedance approach. Lift/thrust decoupling conditions are investigated in Section 4. The dynamic model of MAV and the structure of designed controllers are discussed in Sections 5 and 6, respectively. Results of simulated flight experiments are presented in Section 7. Finally, Section 8 concludes this paper.

2 Mechanical Impedance of the Wing Joint

In [23], we reviewed the different types of muscle that most insects employ during flight. Among them, synchronous muscles [21] are the only kind that is directly attached to the wing joint. Thus, they should have a key role in determining mechanical impedance of the wing joint. This mechanical impedance is responsible for regulation of changes in wing's angle of attack (AoA) in response to aerodynamic torques [20]. Thus, modeling these muscles could further improve our understanding of insect flight.

2.1 Muscle-Joint Connection: Mechanical Model

The antagonistic synchronous muscle pairs in Fig. 2 [27] and their connection to the wing joint can be modeled by the mechanical structure illustrated in Fig. 3. The behavior of each muscle can be approximately modeled by a quadratic spring [28], i.e. its output force F is equal to:

$$F(\delta_i) = \frac{1}{2} A\delta_i^2 + B\delta_i + C,\ i = 1, 2 \tag{1}$$

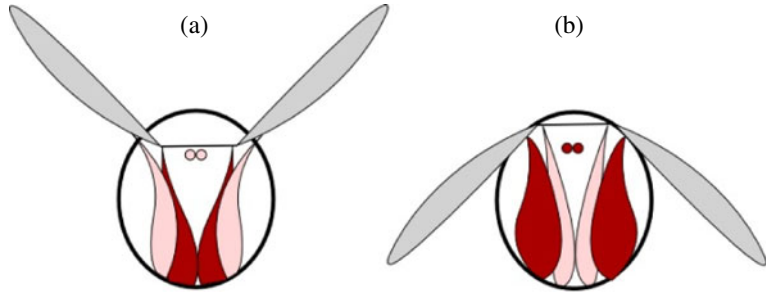

Fig. 2 An illustration of insect's wing stroke using synchronous muscles: **a** upstroke and **b** downstroke. Muscles in the process of contraction are shown in a darker color (adapted from [27])

where A, B and C are constant coefficients and δ_i represent the corresponding change in length of each spring.

In [23], using Eq. 1 we have shown that rotational stiffness of the joint in Fig. 3 is derived as:

$$k_{\text{rot}} = 2R^2 (Ax_c + B) \tag{2}$$

Here, R is the radius of the joint and x_c represents the displacement due to co-activation of antagonistic muscle pair, i.e.:

$$x_c = \frac{1}{2}(x_1 + x_2) \tag{3}$$

The displacement induced by actuator force F_{Mi} on the input end of each spring is shown by x_i. The differential displacement of these springs, i.e. x_d, is responsible for adjustment of wing's equilibrium pitch angle ψ_0:

$$x_d = \frac{1}{2}(x_1 - x_2) = R\psi_0 \tag{4}$$

It was also shown [23] how an external torque τ_{ext} influences the pitch angle ψ of the wing joint:

$$\tau_{\text{ext}} = k_{\text{rot}} (\psi - \psi_0) \tag{5}$$

Hence, the wing joint can be considered as a torsional spring whose stiffness k_{rot} and equilibrium point ψ_0 are respectively controlled through co-activation and differential activation of an antagonistic synchronous muscle pair. In Section 3 we show how these parameters influence lift and thrust production.

2.2 Active Impedance Regulation: Power Requirements

Contraction of synchronous muscle pairs may change both stiffness and equilibrium position of the wing joint. Like all other muscles, these contractions consume energy. In Fig. 3, integration of Eq. 1 with respect to δ_i shows how much work W is required to change the length of each spring:

$$W(\delta_i) = \frac{1}{6}A\delta_i^3 + \frac{1}{2}B\delta_i^2 + C\delta_i,\ i = 1, 2 \tag{6}$$

Since:

$$\delta_1 = x_c - R(\psi - \psi_0) \tag{7}$$

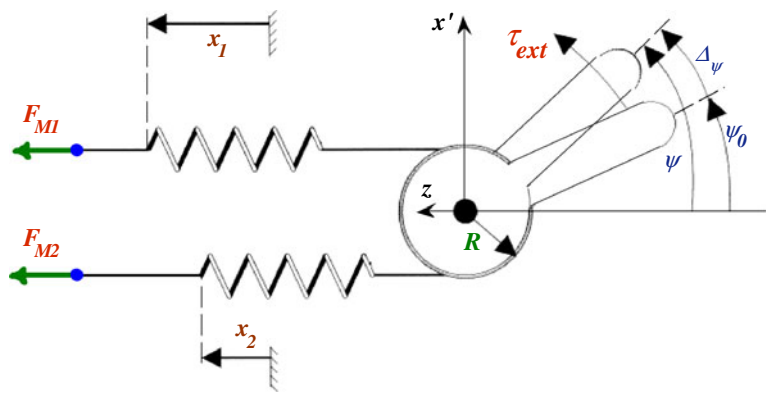

Fig. 3 A simplified mechanical model of synchronous muscle-joint structure. Each muscle is modeled by a quadratic spring. A force of F_{Mi} pulls the input end of each spring, resulting in the displacement x_i. The other sides of both springs are attached to a pulley of radius R which models the joint

$$\delta_2 = x_c + R\left(\psi - \psi_0\right) \tag{8}$$

from Eqs. 2 to 4 the overall work is equal to:

$$W\left(\delta_1\right) + W\left(\delta_2\right) = 2W\left(x_c\right) + \frac{1}{2}k_{\text{rot}}\left(\psi - \psi_0\right)^2 \tag{9}$$

The required power for impedance manipulation, i.e. P_{TI} is then calculated by differentiating Eq. 9 with respect to time:

$$P_{\text{TI}} = 2F\left(x_c\right)\dot{x}_c + \frac{1}{2}\dot{k}_{\text{rot}}\left(\psi - \psi_0\right)^2 - k_{\text{rot}}\left(\psi - \psi_0\right)\dot{\psi}_0 \tag{10}$$

Using Eqs. 1 and 2, it is easy to show that choosing $C = 0.5B^2/A$:

$$F\left(x_c\right)\dot{x}_c = \frac{1}{16A^2R^6}k_{\text{rot}}^2\dot{k}_{\text{rot}} \tag{11}$$

which is then replaced in Eq. 10 to yield:

$$P_{\text{TI}} = \frac{1}{8A^2R^6}k_{\text{rot}}^2\dot{k}_{\text{rot}} + \frac{1}{2}\dot{k}_{\text{rot}}\left(\psi - \psi_0\right)^2 - k_{\text{rot}}\left(\psi - \psi_0\right)\dot{\psi}_0 \tag{12}$$

The last expression allows us to estimate power requirements for manipulation of k_{rot} and ψ_0 based on instantaneous values of these parameters and their time derivatives. In Section 7, we will use Eq. 12 for power estimation during simulated flight experiments with Tunable Impedance controller.

3 The Aerodynamic Model

With low Reynolds numbers, aerodynamics of insect flight has become an active field of research over the past several decades [2–7, 29–31]. Various unsteady-state mechanisms have been identified that depending on the species, demonstrate different amounts of contribution to production of aerodynamic forces. Among these phenomena, three mechanisms are the most significant in many flying insects: *delayed stall* [4], *rotational circulation* [3, 4], and *wake capture* [4, 29]. Experimental data have been used to develop mathematical expressions for estimation of forces produced by these mechanisms [4, 19, 32]. We have previously used these results to model the overall aerodynamic force in a hummingbird scale flapping-wing MAV [23]. Here, we will only repeat the final equations and then proceed to explain the interaction between aerodynamic force and mechanical impedance of the wing joint. Interested readers are encouraged to review [23] for further details on this model.

3.1 Wing Shape and Aerodynamic Forces

The components of aerodynamic force at center of pressure (CoP) of the wing are illustrated in Fig. 4a. In this diagram, pitch angle of the wing is represented by ψ. The stroke profile of the wing—i.e. the angle ϕ in Fig. 4b—is assumed to be sinusoidal:

$$\phi = \phi_0 \cos\left(2\pi f_s t\right) + \beta \tag{13}$$

where ϕ_0 is the magnitude of stroke and f_s represents flapping frequency. β is a slowly varying bias angle and has an insignificant effect on force production [23]. More details on this parameter will be provided in Section 6.

Using the quasi-steady-state aerodynamic model of [23] along with Blade Element Method (BEM) [3, 33, 34], the aerodynamic force for the wing shape in Fig. 5 can be estimated by:

$$F_N = 0.0442\rho\left(C_N\left(\psi\right)\dot{\phi} + 1.3462\dot{\psi}\right)\dot{\phi}R_W^4 \tag{14}$$

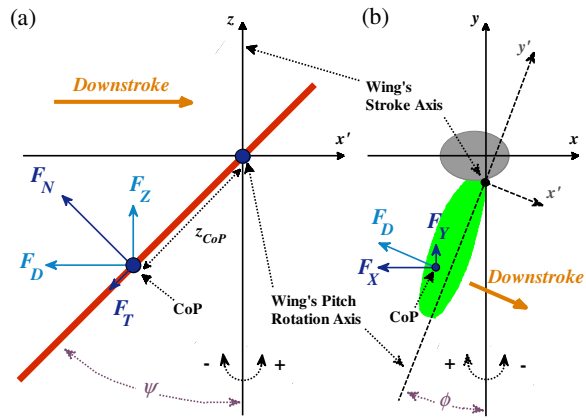

Fig. 4 **a** Wing cross-section (during downstroke) at center of pressure, illustrating the pitch angle ψ. Normal and tangential aerodynamic forces are represented by F_N and F_T. F_Z and F_D represent the lift and drag components of the overall force. **b** Overhead view of the wing/body setup which demonstrates the stroke angle ϕ. F_X and F_Y are components of F_D which represent forward and lateral thrust, respectively

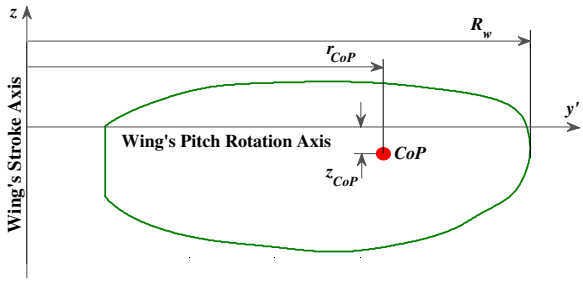

Fig. 5 The wing shape used in aerodynamic model and flight simulations. The span of the wing is represented by R_w

$$F_T = 0.0442\rho C_T(\psi)\dot{\phi}^2 R_W^4 \tag{15}$$

where ρ is the density of air and R_W represents the span of the wing. As illustrated in Fig. 4a, F_N and F_T are the normal and tangential components of the overall aerodynamic force with respect to the surface of the wing. C_N and C_T are angle-dependent aerodynamic coefficients [4, 23]:

$$C_N(\psi) = 3.4\cos\psi \tag{16}$$

$$C_T(\psi) = \begin{cases} 0.4\cos^2(2\psi), & |\psi| \geq \dfrac{\pi}{4}\ rad \\ 0, & otherwise \end{cases} \tag{17}$$

Lift F_Z and drag F_D components of the aerodynamic force are calculated as follows:

$$F_Z = -F_N\sin\psi - F_T\cos\psi \tag{18}$$

$$F_D = -F_N\cos\psi + F_T\sin\psi \tag{19}$$

Forward and lateral thrust, i.e. F_X and F_Y, respectively, are also defined as illustrated in Fig. 4b:

$$F_X = F_D\cos\phi \tag{20}$$

$$F_Y = -F_D\sin\phi \tag{21}$$

Finally, it is important to note that the center of pressure [23] in Fig. 5 is located at:

$$z_{\text{CoP}} = 0.0673\,R_W \tag{22}$$

$$r_{\text{CoP}} = 0.7221\,R_W \tag{23}$$

3.2 The Tunable Impedance Approach: A Review

As it was stated in Section 2.1, mechanical impedance properties of the joint tend to oppose any external torque on the wing according to Eq. 5. Aerodynamic force and dynamics of the wing influence the rotation of the wing via the following torque expression:

$$\tau = z_{\text{CoP}}F_N - b_\psi\dot{\psi} - J_\psi\ddot{\psi} \tag{24}$$

in which J_ψ and b_ψ are the moment of inertia and passive damping coefficient of the wing along its pitch rotation axis, respectively. As illustrated in Fig. 5, z_{CoP} is the distance of CoP from this axis.

According to Newton's Equations of Motion, the left-hand sides of Eqs. 5 and 24 must be equal, hence resulting in:

$$J_\psi\ddot{\psi} + b_\psi\dot{\psi} + k_{\text{rot}}(\psi - \psi_0) - z_{\text{CoP}}F_N = 0 \tag{25}$$

Using the presented aerodynamic model in Section 3.1, Eq. 25 can be numerically solved to calculate changes in ψ and F_N for any stroke profile and mechanical impedance values. Other aerodynamic profiles will then be available via Eq. 15 and Eqs. 18–21.

The values of wing parameters used in all future simulations are reported in Table 1. Since the employed MAV model is roughly the same size as an average hummingbird, stroke parameters

Table 1 Physical characteristics used in Section 3

Symbol	Description	Value
ρ	Air density at sea level	1.28 kg· m^{-3}
R_W	Average span of each wing in an average hummingbird	8×10^{-2} m
J_ψ	Moment of inertia of each wing (pitch rotation)	1.564×10^{-8} N· m· s^2
b_ψ	Passive damping coefficient of each wing (pitch rotation)	5×10^{-6} N· m· s
m_{body}	Estimated mass of a two-winged MAV with dimensions of an average hummingbird	4×10^{-3} kg
g	Standard gravity at sea level	9.81 m· s^{-2}

during hovering flight are set to $\phi_0 = 60°$ and $f_s = 25$ Hz [21]. Similar to a hummingbird, the MAV model has two wings and throughout this work, it is assumed that they have always the same stroke profiles and mechanical impedance properties. Under these assumptions, symmetry dictates that overall lateral thrust and roll/yaw torques are zero; hence motion is effectively limited within the sagittal plane. This allows us to concentrate only on lift F_Z and forward thrust F_X of a single wing. Roll and yaw responses of the model are previously investigated in [23, 26].

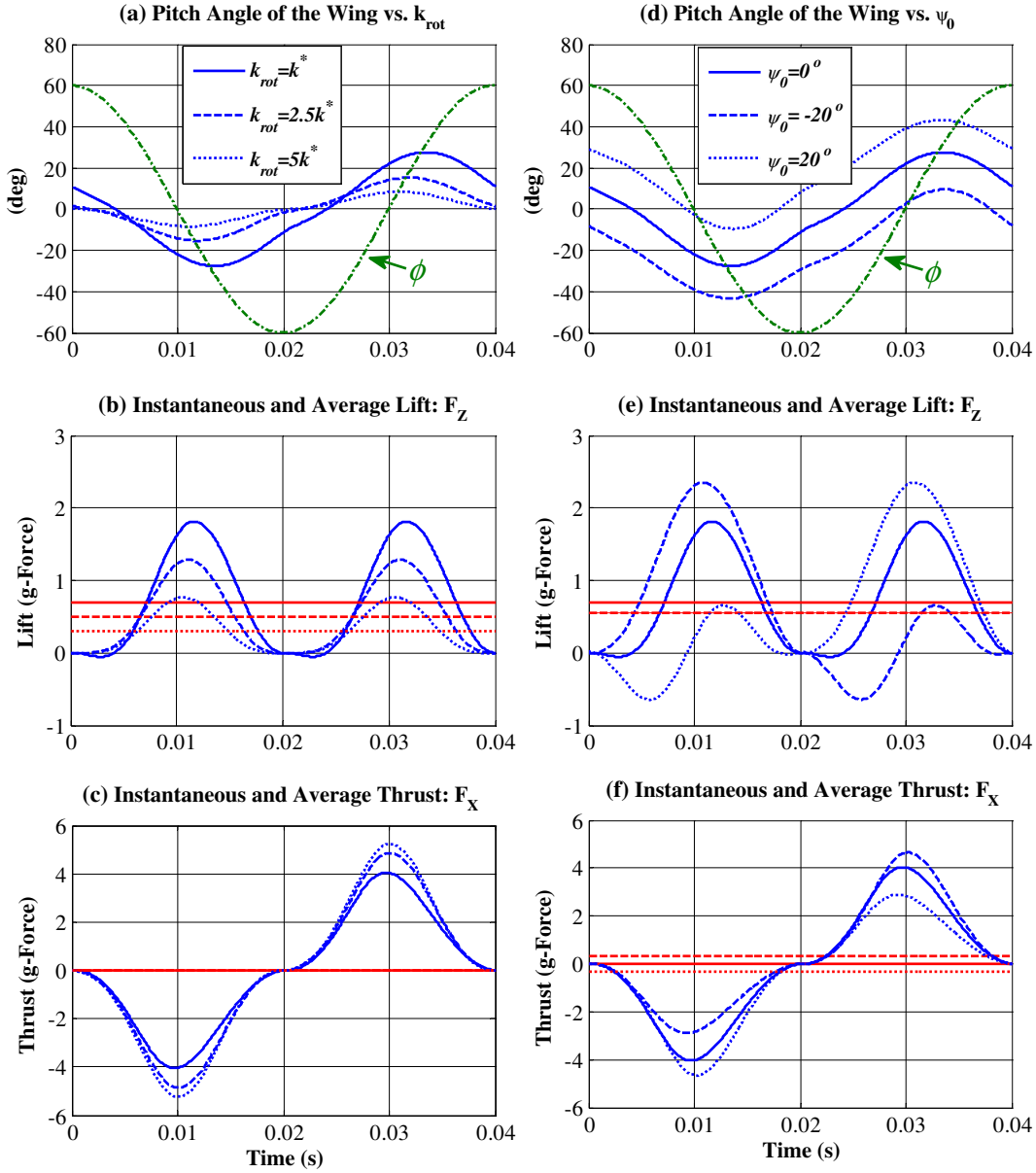

Fig. 6 **a** Pitch angle evolution of one wing for $\psi_0 = 0°$ and different values of k_{rot} ($k^* = 1.5 \times 10^{-3}$ N· m/rad). The corresponding instantaneous (*blue*) and average (*red*) lift and forward thrust are plotted in **b** and **c** respectively. **d** Pitch angle evolution of one wing for $k_{\text{rot}} = k^*$ and different values of ψ_0. The corresponding instantaneous (*blue*) and average (*red*) lift and forward thrust are plotted in **e** and **f**, respectively. All forces are normalized by the estimated weight of the vehicle

The tunable impedance approach suggests that by modification of impedance properties, one can manipulate pitch profile of either wing while its stroke profile remains unperturbed. In fact, the value of k_{rot} primarily determines the range of variations in ψ (Fig. 6a) which in turn affects the magnitude of aerodynamic forces (Fig. 6b, c). Note that when $\psi_0 = 0°$, pitch and thrust profiles are odd-symmetric, i.e. the average thrust is close to 0. Introducing a nonzero value of ψ_0 perturbs this symmetry (Fig. 6f) by biasing the pitch profile (Fig. 6d). In short, tunable impedance allows us to control overall lift and thrust by manipulating k_{rot} and ψ_0, respectively [23]. From Fig. 6, although instantaneous forces are time-dependent, their average values remain constant as long as mechanical impedance properties and stroke parameters are unperturbed. We can use these mean values to further investigate the influence of impedance/stroke parameters in lift/thrust production.

Figure 7a, b illustrate the changes in mean F_Z and F_X of a single wing as various k_{rot} and ψ_0 pairs are examined. All force values are normalized by the weight of the model. At $\psi_0 = 0°$, instantaneous forward thrust has an approximately zero mean value regardless of the selected k_{rot} (Fig. 7c). On the other hand, mean value of lift significantly varies as k_{rot} is changed. Particularly, when $k_{\text{rot}} = k_{\text{op}} = 3.92 \times 10^{-3}$ N· m/rad, two wings will be able to produce just enough lift to levitate the model – i.e. 0.5 g-Force per wing. Therefore, we choose this point as the nominal mechanical impedance values for hovering. Note that when $k_{\text{rot}} = k_{\text{op}}$, small changes in ψ_0 slightly influence mean lift but also result in significant nonzero values of mean thrust (Fig. 7d).

From Fig. 7c, d, around $k_{\text{rot}} = k_{\text{op}}$ and $\psi_0 = 0°$, average lift and thrust are respectively proportional to stiffness and equilibrium angle ψ_0 of the joint. Using these relationships, the Tunable Impedance method enables the model to regulate

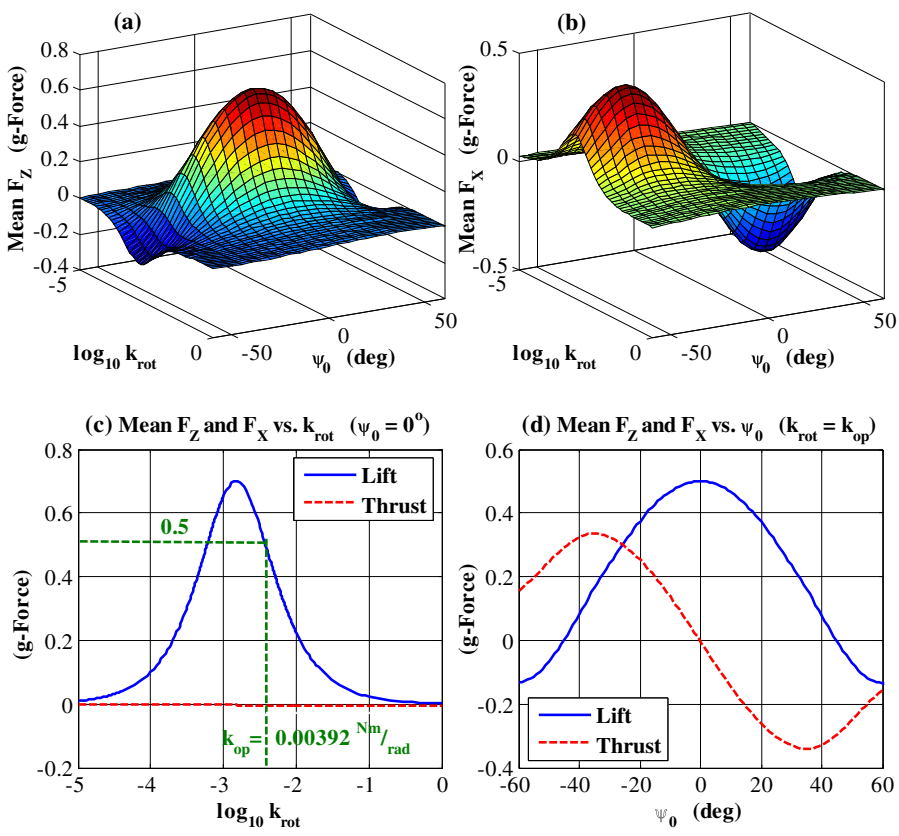

Fig. 7 **a** Mean F_Z vs. k_{rot} and ψ_0. **b** Mean F_X vs. k_{rot} and ψ_0. **c** Mean values of F_Z and F_X vs. k_{rot} when $\psi_0 = 0°$. At $k_{\text{rot}} = k_{\text{op}} = 3.92 \times 10^{-3}$ N· m/rad, two wings are able to produce just enough lift to levitate the model. **d** Mean values of F_Z and F_X vs. ψ_0 when $k_{\text{rot}} = k_{\text{op}}$. All force values are normalized by the weight of the model. Stroke profile is always sinusoidal with constant parameters: $\phi_0 = 60°$ and $f_s = 25$ Hz

aerodynamic forces during various agile flight maneuvers [23]. However, Fig. 7 also demonstrates that lift and thrust are influenced by both mechanical impedance parameters. Therefore, an attempt to control one force through adjustment of the corresponding mechanical impedance parameter may result in perturbation of the other force, thus complicating simultaneous control of both forces. In Section 4 we will investigate possible conditions that reduce the coupling between lift and thrust forces, hence allowing us to employ simpler control structures.

The present work also concentrates on flight efficiency and power requirements of the Tunable Impedance approach. To do so, our proposed method will be compared to a conventional ad hoc control approach that manipulates frequency and shape of the stroke profile to adjust production of aerodynamic forces. From Eqs. 13–15, the magnitude of overall instantaneous aerodynamic force is approximately a quadratic function of f_s. This relationship can also be observed in Fig. 8a where changes in mean lift and thrust vs. f_s are plotted for a single wing. Note that in this case, mechanical impedance properties are always constant, i.e. $k_{\text{rot}} = k_{\text{op}}$ and $\psi_0 = 0°$.

From this diagram, stroke frequency can be used to control lift. However, mean thrust is unaffected by changes in f_s. Note that as long as $\psi_0 = 0°$ and ϕ has a perfect sinusoidal waveform, thrust profile over one stroke cycle remains odd-symmetric [23]. Therefore, mean thrust will be close to zero. One way of producing nonzero thrust values is to employ asymmetric stroke profiles. This method is also known as *Split Cycle* [15]. Normally, upstroke and downstroke in one cycle take the same amount of time, hence their individual mean thrusts are equal and in opposite directions. By increasing the flapping speed in one part and reducing it in the other one, it is possible to disturb this balance and create forward or backward thrust. To this end, we define T_{ds} as the ratio of time spent in downstroke to duration of the full stroke cycle. By definition, $T_{\text{ds}} = 0.5$ is equivalent to a symmetric stroke profile and zero mean thrust. Figure 8b shows that a 20 % change in this value slightly increases mean lift, but at the same time, a mean thrust of approximately 0.25 g-Force per wing will be achievable. Hence, simultaneous manipulation of f_s and T_{ds} can be used as a direct approach to force/motion control in flapping-wing MAVs.

4 Decoupling Conditions for Lift/Thrust Control

To investigate the possibility of decoupled lift/thrust control via tunable impedance approach, we first revisit the diagrams in Fig. 7. From Fig. 7a and d, small changes in the value of ψ_0 have little influence on overall lift. Similarly, Fig. 7b, c show that small changes in k_{rot} around k_{op} only

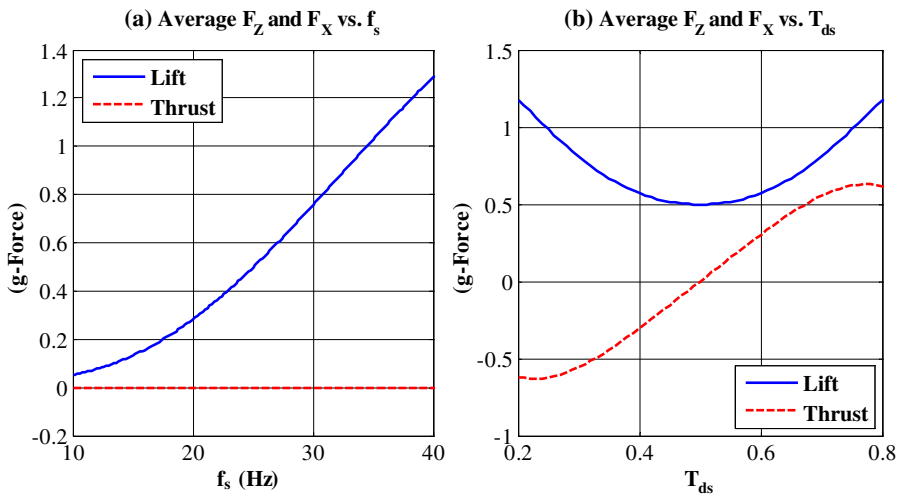

Fig. 8 **a** Mean values of F_Z and F_X vs. f_s when $T_{\text{ds}} = 0.5$. At $f_s = 25$ Hz, two wings are able to produce just enough lift to levitate the model. **b** Mean values of F_Z and F_X vs. T_{ds} when $f_s = 25$ Hz. All force values are normalized by the weight of the model. Mechanical impedance parameters are always constant: $k_{\text{rot}} = k_{\text{op}}$ and $\psi_0 = 0°$

slightly affect overall thrust. Hence, as a trade-off between these characteristics and production of sufficiently large forces, we have chosen to limit the mechanical impedance parameters such that $k_{\text{rot}} \in [0.2, 2] \times 10^{-2}$ N·m/rad and $|\psi_0| \leq 20°$.

The force values in Fig. 7 are calculated for constant impedance parameters. However, the linear relationships between steady-state values suggest that a linearized model around $k_{\text{rot}} = k_{\text{op}}$ and $\psi_0 = 0°$ will be able to provide a reasonable approximation of dynamic behavior of these forces in response to varying impedance properties. To find this linear model, we employ system identification techniques—computation/smoothing of Empirical Transfer Function Estimates followed by subspace identification method [35] for transfer function matching—in order to estimate the components of nonlinear MIMO system that relates impedance parameters to aerodynamic forces:

$$\delta F_Z(s) = G_{ZK}(s)\,\delta K(s) + \Delta_{Z\Psi}(s) \tag{26}$$

$$\delta F_X(s) = (1 + \Delta_{XK}(s))\,G_{X\Psi}(s)\,\psi_0(s) \tag{27}$$

δF_Z and δF_X respectively represent the changes in average lift and forward thrust due to variations of k_{rot} and ψ_0 values around $k_{\text{rot}} = k_{\text{op}}$ and $\psi_0 = 0°$. Note that $\delta K = \log_{10}(k_{\text{rot}} / k_{\text{op}})$. G_{ZK} is the transfer function that relates δK to average lift while $G_{X\Psi}$ represents the transfer function from ψ_0 to average thrust. The impact of ψ_0 variations on average lift and stiffness variations on average thrust are modeled by disturbance terms $\Delta_{Z\Psi}$ and Δ_{XK}, respectively. Figure 9 illustrates a closer look at Fig. 7a, b around the chosen operation point. These diagrams support our particular choice of disturbance terms in Eqs. 26 and 27.

In all system identification experiments, limits of $|\delta K| < 0.05$ and $|\psi_0| < 0.1$ rad have been enforced. The Bode diagrams of identified transfer functions are plotted in Fig. 10. Figure 11 illustrates the frequency profile of maximum gain from each mechanical impedance parameter to the corresponding disturbance term. In low frequencies, both G_{ZK} and $G_{X\Psi}$ have steady-state gains close to 0 dB, while in comparison, the maximum gains in Fig. 11 are well below unity. Therefore, we expect that simultaneous manipulation of mechanical impedance parameters in the low frequency range has a less perturbing effect on individual lift and thrust control mechanisms.

To choose a suitable upper limit for this range, three groups of numerical experiments have been conducted. In the first group, sinusoidal waves of magnitude 0.05 and various frequencies were used for δK while ψ_0 was set to 0 rad. In this case, changes in average lift and thrust are respectively treated as ideal F_{Zi} and disturbance F_{Xd}. In the second group, sinusoidal waves of magnitude 0.1 rad and various frequencies were used for ψ_0 while k_{rot} was kept at k_{op}. In this case, changes in average lift and thrust are respectively treated as disturbance F_{Zd} and ideal F_{Xi}. Finally, the

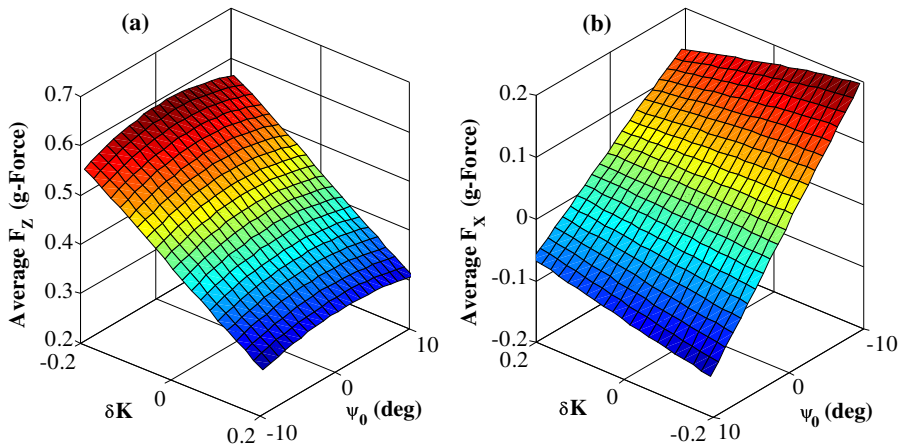

Fig. 9 **a** Average lift for impedance values around $k_{\text{rot}} = k_{\text{op}}$ and $\psi_0 = 0°$. **b** Average thrust for impedance values around $k_{\text{rot}} = k_{\text{op}}$ and $\psi_0 = 0°$. All force values are normalized by the estimated weight of the vehicle. Note that $\delta K = \log_{10}(k_{\text{rot}}/k_{\text{op}})$

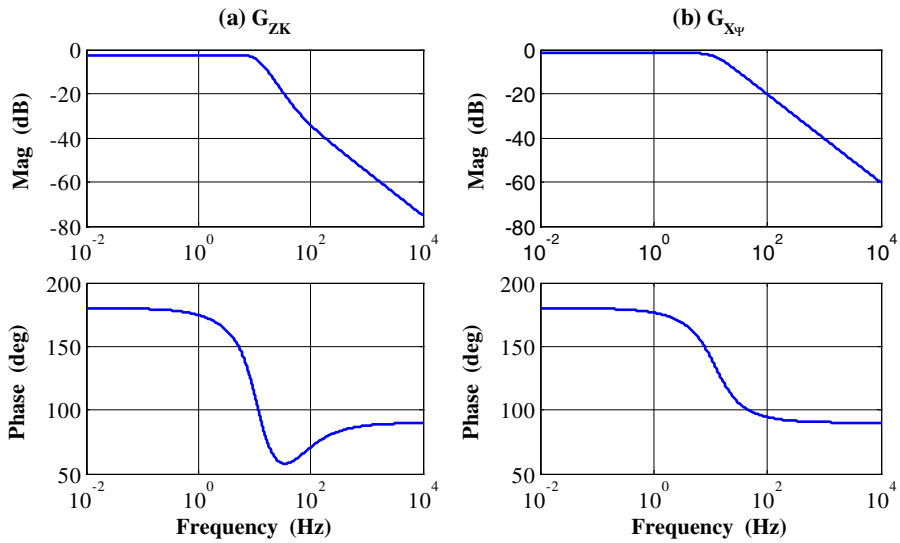

Fig. 10 Bode diagrams of the identified transfer functions **a** from δK to average lift, i.e. G_{ZK} and **b** from ψ_0 to average thrust, i.e. $G_{X\Psi}$

third group of experiments uses both described nonzero inputs at the same time. Lift and thrust changes in this group are the overall results of impedance manipulation, i.e. F_{Zo} and F_{Xo}. The frequency profiles of correlation between ideal (disturbance) and overall lift outputs are plotted in Fig. 12a, b. Similarly, frequency profiles of correlation between ideal (disturbance) and overall thrust outputs are plotted in Fig. 12c, d.

From Fig. 12, when the frequency content of both inputs is below 10 Hz, the correlation between ideal and overall profile of either force is above 0.917 while the correlation between disturbance and overall values remains below 0.239. Thus, by employing low-pass filters to remove the frequency content of δK and ψ_0 above 10 Hz, coupling between lift and thrust manipulation could be reduced significantly.

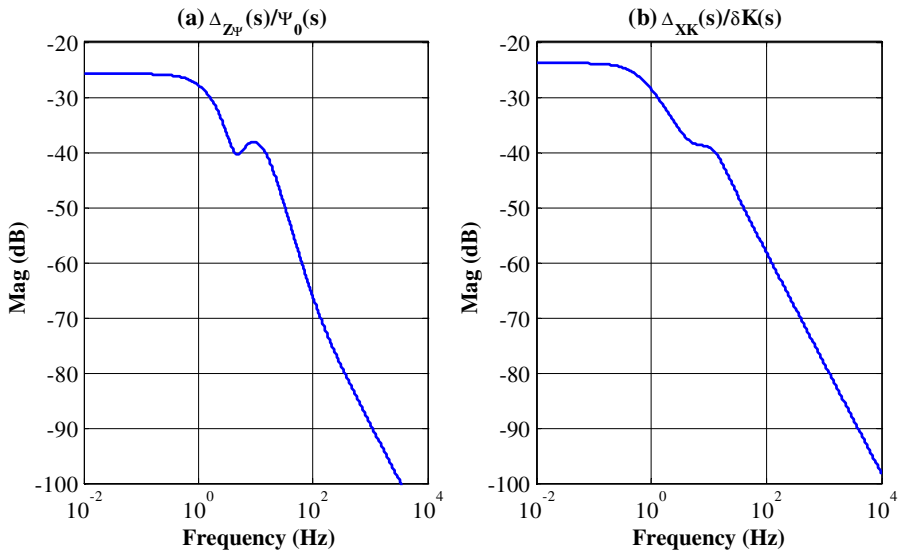

Fig. 11 Frequency profile of maximum gain **a** from ψ_0 to lift disturbance $\Delta_{Z\Psi}$ and **b** from δK to thrust disturbance Δ_{XK}

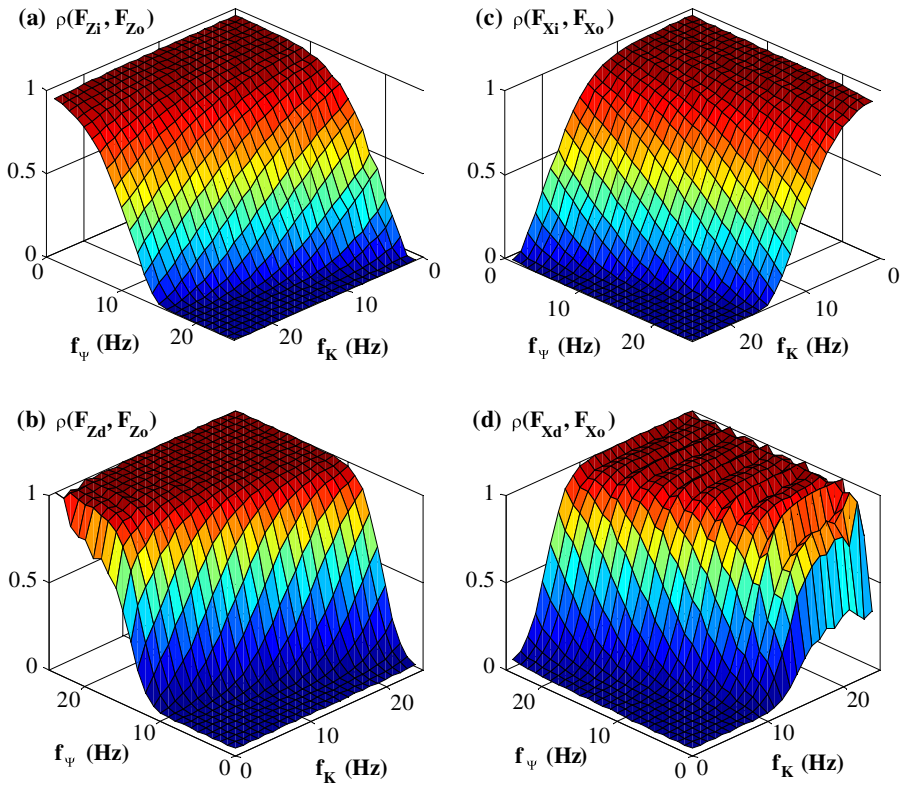

Fig. 12 Correlation coefficient vs. frequency of mechanical impedance manipulation for **a** F_{Zi} and F_{Zo}, i.e. ideal and overall lift, **b** F_{Zd} and F_{Zo}, i.e. disturbance and overall lift, **c** F_{Xi} and F_{Xo}, i.e. ideal and overall thrust, **d** F_{Xd} and F_{Xo}, i.e. disturbance and overall thrust. Here, f_Ψ and f_K respectively represent the frequency of employed sinusoidal signals for ψ_0 and δK

5 Dynamic Model of the Flapping-Wing MAV

The free-body diagram of a typical two-winged flapping-wing MAV model is illustrated in Fig. 13. This body structure is inspired the proposed vehicle in [9]. The shape of each wing is as demonstrated in Fig. 5 while its other characteristics are as reported in Table 1.

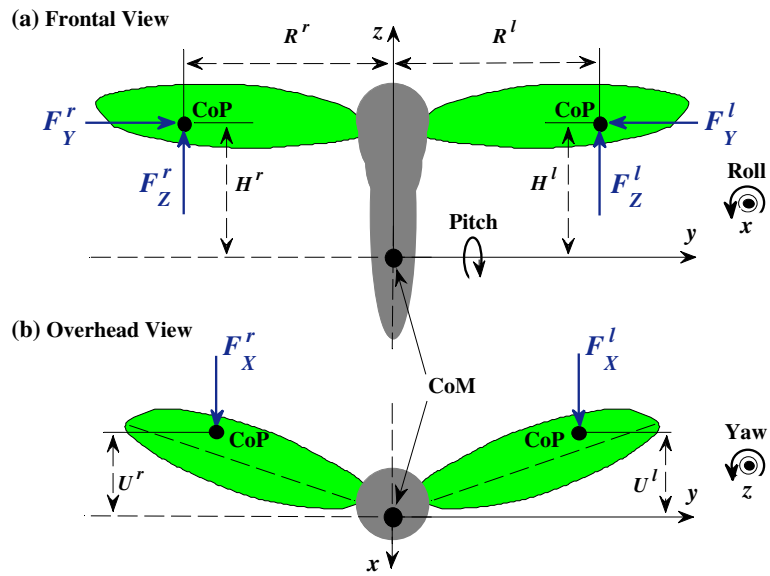

Fig. 13 Free-body diagram of a two-winged flapping-wing MAV: **a** frontal and **b** overhead views. H, R and U are the distance components of center of pressure (CoP) of each wing from center of mass (CoM) of the model. For simulation purposes, Euler angles in Tait-Bryan XYZ convention are employed to update the orientation of the body

Through employing Newton's equations of motion, a six degree-of-freedom (DoF) mathematical model can be derived in this body frame [19]:

$$m_{\text{body}}\left(\dot{\vec{v}}+\vec{\omega}\times\vec{v}\right)=\vec{F}^{l}+\vec{F}^{r}-m_{\text{body}}\vec{G}-b_{v}\,|\vec{v}|\,\vec{v} \tag{28}$$

$$J_{\text{body}}\dot{\vec{\omega}}+\vec{\omega}\times J_{\text{body}}\vec{\omega}=\vec{D}^{l}\times\vec{F}^{l}+\vec{D}^{r}\times\vec{F}^{r}-b_{\omega}\vec{\omega} \tag{29}$$

where:

$$\vec{F}^{l}=\begin{bmatrix}F_{X}^{l}\\-F_{Y}^{l}\\F_{Z}^{l}\end{bmatrix},\ \vec{F}^{r}=\begin{bmatrix}F_{X}^{r}\\F_{Y}^{r}\\F_{Z}^{r}\end{bmatrix} \tag{30}$$

and:

$$\vec{D}^{l}=\begin{bmatrix}U^{l}\\R^{l}\\H^{l}\end{bmatrix},\ \vec{D}^{r}=\begin{bmatrix}U^{r}\\-R^{r}\\H^{r}\end{bmatrix} \tag{31}$$

Here, translational and angular velocities of the MAV's body are represented by vectors $\boldsymbol{v}$ and $\boldsymbol{\omega}$, respectively. H, R and U are the distance components of center of pressure of each wing from the overall center of mass (CoM), as shown in Fig. 13. Superscripts r and l respectively refer to the right and left wings. The vector $\boldsymbol{G}$ expresses gravity in the body coordinate frame. To keep track of the orientation of the body with respect to the reference coordinates, Euler angles in the Tait-Bryan XYZ convention are employed. The coefficient of viscous friction is represented by b_v while the parameter b_ω is used to model the effect of passive rotational damping, as discussed in [36].

Mass of the body, i.e. m_{body}, is assumed to be 4×10^{-3} kg for a vehicle of desired scale (Table 1). The body shape in Fig. 13 is chosen since its corresponding inertia matrix relative to the center of mass (CoM), i.e. J_{body}, has insignificant nondiagonal terms and thus, can be approximated by:

$$J_{\text{body}}=\begin{bmatrix}J_{\text{roll}}&0&0\\0&J_{\text{pitch}}&0\\0&0&J_{\text{yaw}}\end{bmatrix} \tag{32}$$

where J_{roll}, J_{pitch} and J_{yaw} are the body's individual moments of inertia around x, y and z axes, respectively. All related physical parameters of the body are listed in Table 2.

6 Flight Controllers

Based on the discussions in Section 3.2, two different controllers are developed to control the simulated flight of dynamic model described in Section 5. As it was noted earlier, motion of the model will be restricted within sagittal plane, hence both controllers only deal with regulation of lift and forward thrust forces. In the remainder of this section, we will review the details and structure of these controllers.

Table 2 Physical Characteristics of the modeled MAV's body

Symbol	Description	Value
b_ω	Passive damping coefficient of the body (rotation)	3×10^{-3} N· m· s
b_v	Viscous friction coefficient of the body when moving in the air	4×10^{-4} N· m^{-2}· s^2
$J_{\text{pitch}}=J_{\text{roll}}$	Pitch and roll moments of inertia of the body relative to CoM	4.38×10^{-6} N· m· s^2
J_{yaw}	Yaw moment of inertia of the body relative to CoM	1.15×10^{-7} N· m· s^2
$H(\psi=0°)$	Distance of CoP from axial plane of the body (xy in Fig. 13) when $\psi=0°$	2.89×10^{-2} m
$R(\phi=0°)$	Distance of CoP from sagittal plane of the body (xz in Fig. 13) when $\phi=0°$	5.78×10^{-2} m
$U(\phi=0°)$	Distance of CoP from coronal plane of the body (yz in Fig. 13) when $\phi=0°$	5.8×10^{-3} m
W_{body}	Body width at the base of wings	1.16×10^{-2} m

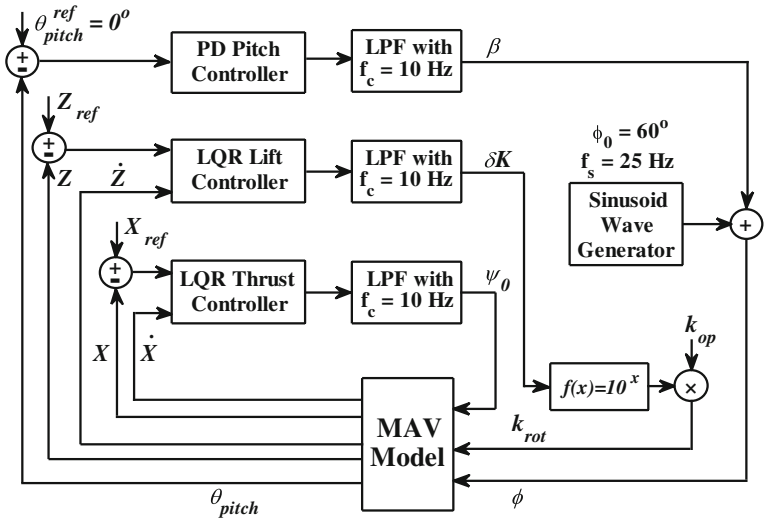

Fig. 14 Block diagram of the proposed Tunable Impedance motion controller in interaction with MAV model. Cutoff frequency f_c of each low-pass filter is set to 10 Hz. Both wings employ similar values of β, k_{rot} and ψ_0 at all times. The stroke profile properties are always constant: i.e. $\phi_0 = 60°$, $f_s = 25$ Hz and $T_{\text{ds}} = 0.5$

6.1 Controller 1: Tunable Impedance Approach

The block diagram in Fig. 14 shows how the Tunable Impedance controller is structured. To calculate appropriate LQR gains, the estimated transfer functions in Section 4 have been used to develop a linear model of the system from mechanical impedance parameters to vertical/horizontal position and velocity. The final result is as follows:

$$\delta K = 25\,(Z - Z_{\text{ref}}) + 2\dot{Z} \tag{33}$$

$$\psi_0 = 2000\,(X - X_{\text{ref}}) + 100\dot{X} \tag{34}$$

where X and Z are respectively the horizontal and vertical positions of the model in sagittal plane. X_{ref} and Z_{ref} define the reference trajectory of motion within this plane. To reduce coupling (Fig. 7 c, d), the outputs of these controllers are chosen to be limited such that $k_{\text{rot}} \in [0.2, 2] \times 10^{-2}$ N·m/rad and $|\psi_0| \leq 20°$. As argued in Section 4, presence of low-pass filters on the controller outputs further improves decoupling [37]. Note that for controller 1, the stroke profile properties of both wings are always constant: $\phi_0 = 60°$, $f_s = 25$ Hz and $T_{\text{ds}} = 0.5$.

Pitch angle of the body θ_{pitch} tends to be unstable. To keep this angle small, i.e. to maintain the

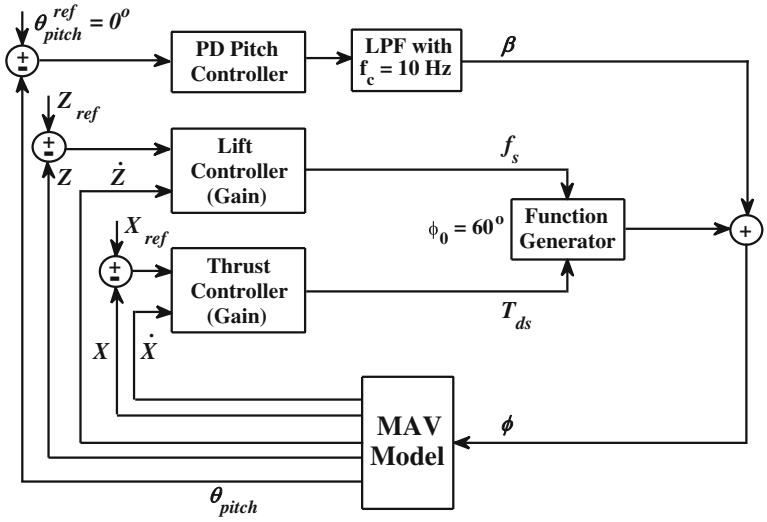

Fig. 15 Block diagram of controller 2 in interaction with MAV model. Both wings employ similar values of β, f_s and T_{ds} at all times. The magnitude of stroke and mechanical impedance parameters are always constant: i.e. $\phi_0 = 60°$, $k_{\text{rot}} = k_{\text{op}}$ and $\psi_0 = 0°$

upright orientation of the model, we chose to bias the stroke profile with a variable amount represented by β. The details of this control mechanism are discussed in [23]. The value of β is adjusted by a PD sub-controller which is tuned to $10 + 0.05s$ through trial and error. The output of this controller is limited such that $|\beta| \leq 15°$.

6.2 Controller 2: Split Cycle and Frequency Manipulation

Figure 15 demonstrates the block diagram of the second controller. In this approach, mechanical impedance parameters are always constant: $k_{\text{rot}} = k_{\text{op}}$ and $\psi_0 = 0°$. Here, lift and forward thrust are respectively controlled through changes in f_s and T_{ds}. The pitch sub-controller in this schematic is identical to the one described earlier for controller 1. The outputs of other sub-controllers are calculated as:

$$f_s = 25 - 187.5\,(Z - Z_{\text{ref}}) - 12.5\dot{Z} \tag{35}$$

$$T_{\text{ds}} = 0.5 - 2.5\,(X - X_{\text{ref}}) - 0.2\dot{X} \tag{36}$$

and are limited to $f_s \in [14.3, 28.5]$ Hz and $T_{\text{ds}} \in [0.4, 0.6]$. The gains in Eqs. 35 and 36 are tuned via trial and error such that in both control methods, simulated responses of the MAV to similar references remain close. The limits on f_s and T_{ds} are imposed to restrict achievable values of

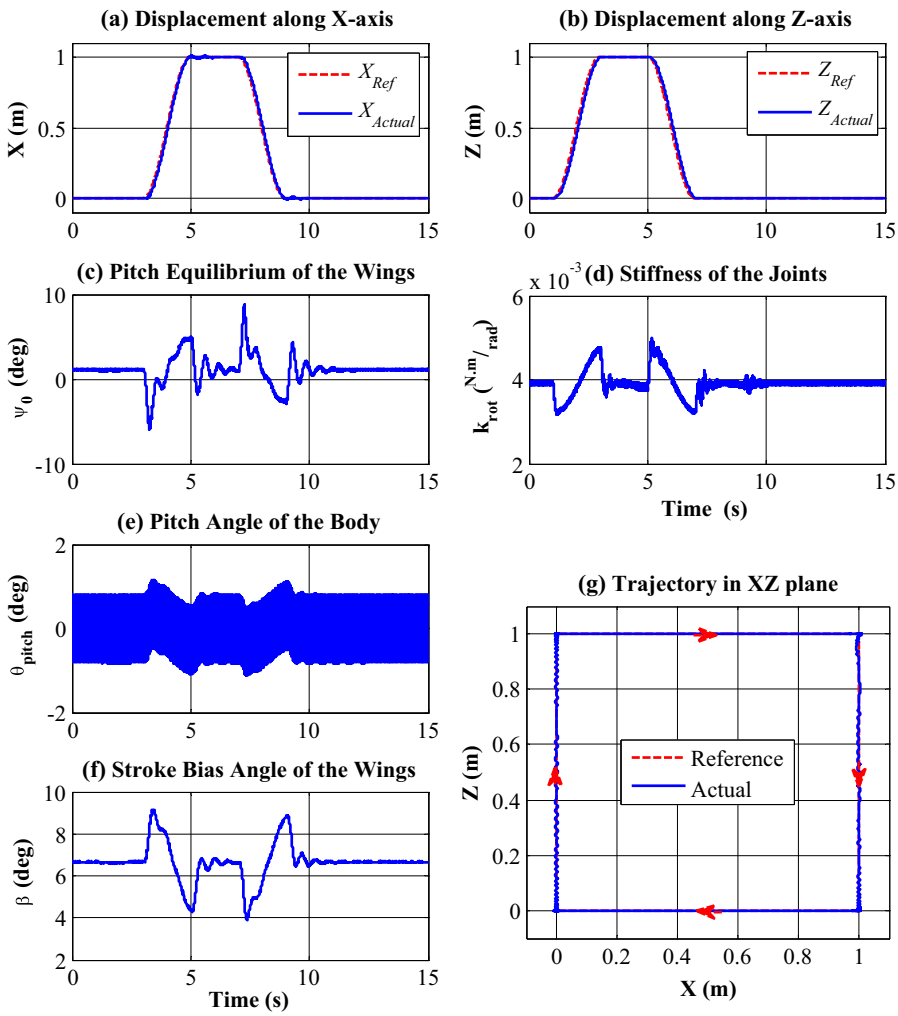

Fig. 16 Simulated results for tracking a square trajectory using controller 1: **a** displacement along X and **b** Z axes, **c** pitch equilibrium of the wings ψ_0, **d** stiffness of the joints k_{rot}, **e** pitch angle of the body θ_{pitch}, **f** stroke bias angle of the wings β and **g** overall trajectory in XZ plane

aerodynamic forces within the same range as controller 1 (Fig. 8a, b).

The output of the function generator in Fig. 15 is originally a sinusoid of constant magnitude $\phi_0 = 60°$ and variable frequency f_s. Depending on the value of T_{ds}, this waveform is further manipulated such that two consecutive half-cycles have appropriate durations.

7 Simulated Experiments

The results of several simulated flight experiments will be discussed in this section. In the first group, we only employ controller 1 to investigate the performance of Tunable Impedance approach and its potential for decoupled control of lift/thrust forces. In the second group, experiments are repeated with both controllers. Overall performance and energy consumption in both cases can then be compared.

7.1 Decoupled Lift/Thrust Control via Tunable Impedance Approach

Using controller 1, motion of the model along various trajectories in the XZ plane has been simulated. In each one of these experiments, the model is initially hovering at $X = 0$ m and $Z = 0$ m, i.e. $X_{\text{ref}} = 0$ m and $Z_{\text{ref}} = 0$ m. Later, new reference position-time profiles are introduced to sub-controllers that guarantee a smooth velocity

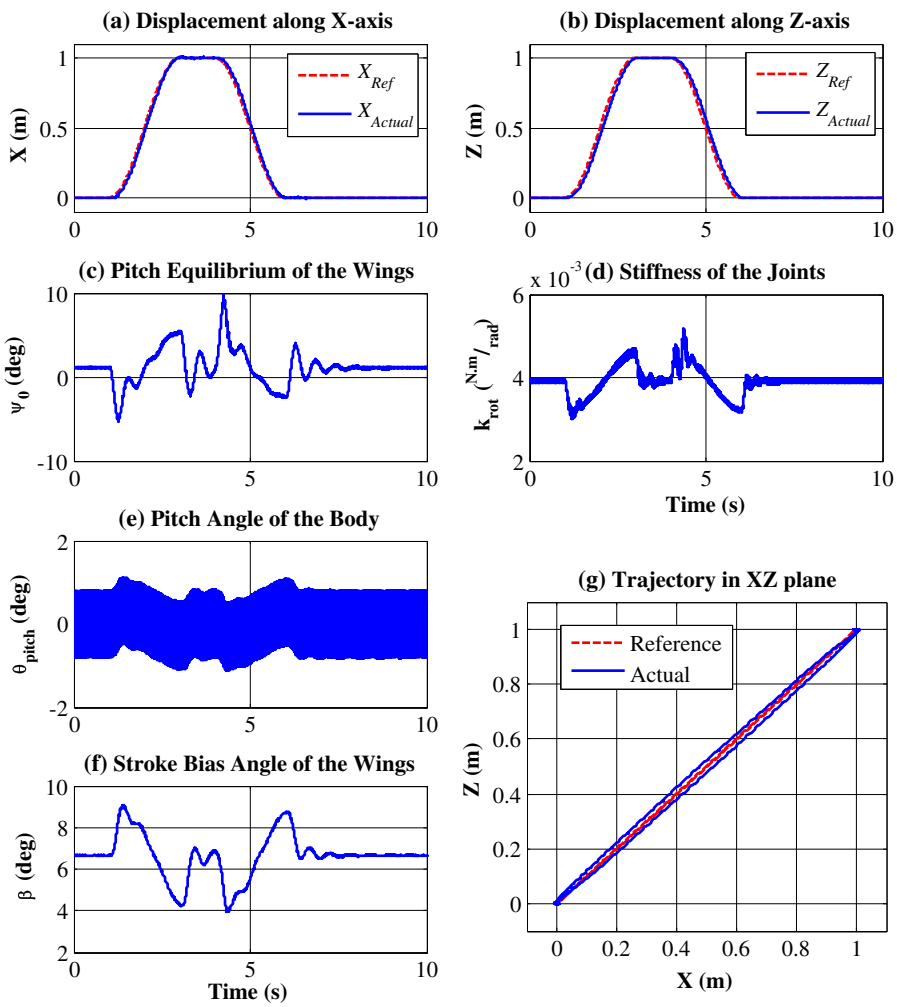

Fig. 17 Simulated results for tracking a linear trajectory with a slope of 1 using controller 1: **a** displacement along X and **b** Z axes, **c** pitch equilibrium of the wings ψ_0, **d** stiffness of the joints k_{rot}, **e** pitch angle of the body θ_{pitch}, **f** stroke bias angle of the wings β and **g** overall trajectory in XZ plane

profile over desired trajectory. We observed that as long as acceleration demands of these profiles are within the capabilities of the model—primarily due to enforced limits on δK and ψ_0—tracking will be achieved with a considerably high degree of precision. The results of simulated experiments with three important types of trajectories are presented next.

7.1.1 Strictly Horizontal (Vertical) Maneuvers

As the most trivial group of maneuvers, the MAV must be able to move along one axis while maintaining a constant position with respect to the other axis. Figure 16 demonstrates the results of tracking a square trajectory that requires a combination of all these maneuvers, i.e. takeoff, landing and forward/backward motion. As it is illustrated, controller 1 successfully handles such maneuvers and keeps the model close to reference trajectory (Fig. 16g). Note that during each sub-maneuver, only one of the mechanical impedance parameters experiences significant changes while the other one remains almost constant (Fig. 16c, d).

7.1.2 Simultaneous Motion along Two Axes: A Linear Trajectory

To further investigate the effectiveness of our proposed approach in decoupling lift and thrust

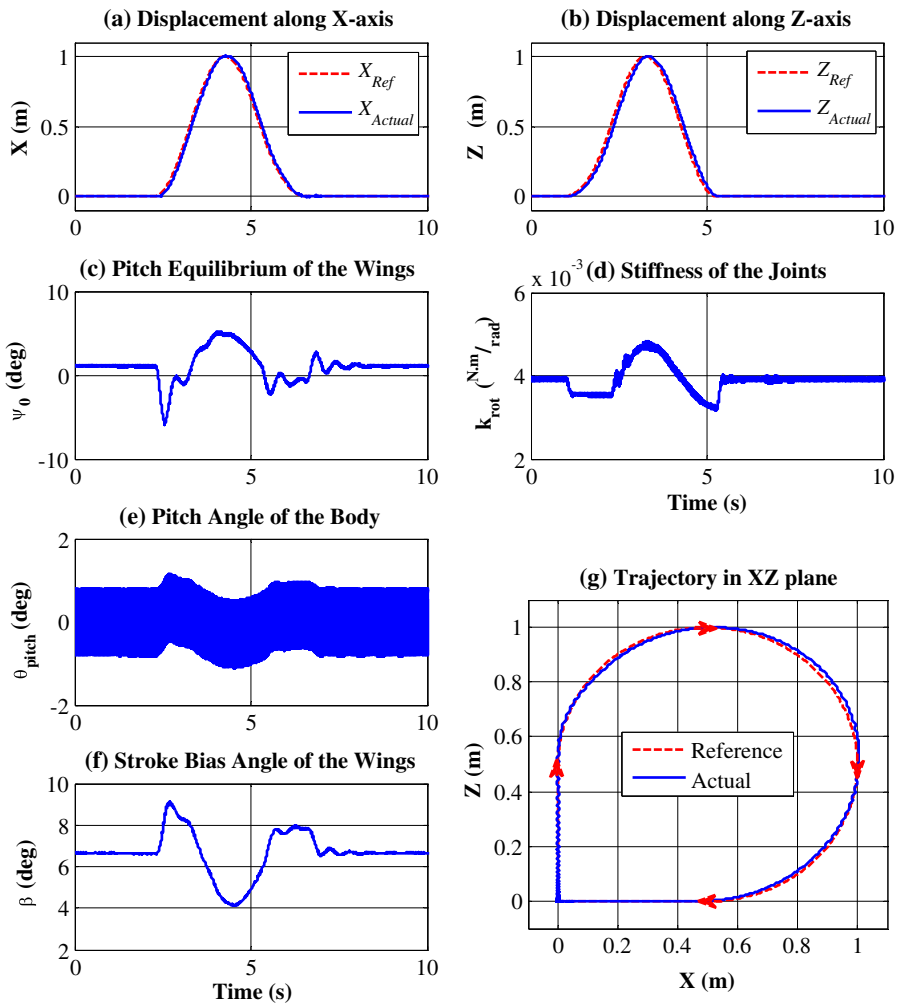

Fig. 18 Simulated results for tracking a partially circular trajectory using controller 1: **a** displacement along X and **b** Z axes, **c** pitch equilibrium of the wings ψ_0, **d** stiffness of the joints k_{rot}, **e** pitch angle of the body θ_{pitch}, **f** stroke bias angle of the wings β and **g** overall trajectory in XZ plane

control, different trajectories with displacements along both X and Z axes were examined. A simple example of such trajectories is a straight line with a slope of 1. Simulation results for the corresponding experiment are illustrated in Fig. 17. A combination of forward flight and takeoff motion starting at $t = 1$ s enables the model to reach $X = 1$ m and $Z = 1$ m by $t = 3$ s. The simulated MAV maintains this position until $t = 4$ s when the direction of motion is reversed. Through simultaneous descent and backward flight, the model returns to its original position at $t = 6$ s. All the while, the slope of its trajectory remains close to 1 (Fig. 17g).

7.1.3 Movement Along Curves

Curves are a more complex case of trajectories with simultaneous displacement along both X and Z axes. The results of an experiment with a partially circular reference trajectory are plotted in Fig. 18. The model still manages to follow this trajectory with reasonable precision (Fig. 18g). Note that compared to other trajectories, correction of motion over curves requires slower changes in impedance parameters (Fig. 18c, d). This is partially due to the fact that stable motion along such trajectories is rarely accompanied by high velocities and/or acceleration rates.

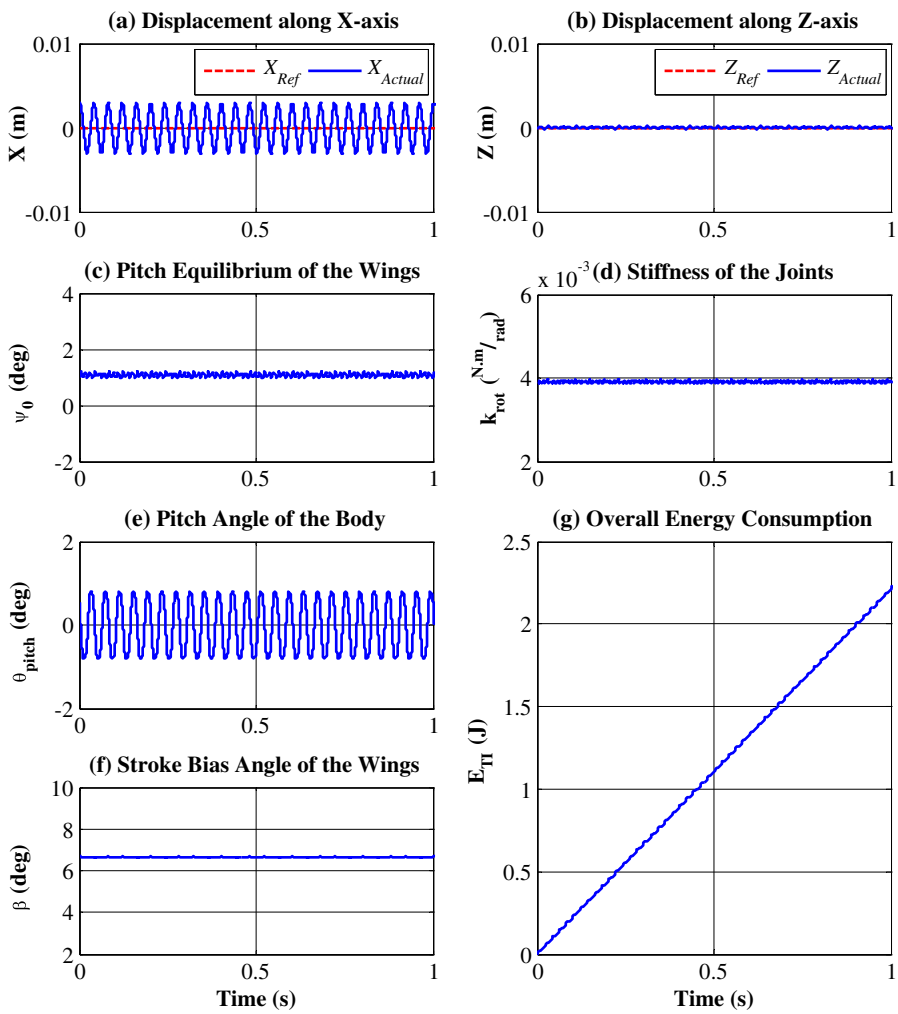

Fig. 19 Simulated results for hovering with controller 1: **a** displacement along X and **b** Z axes, **c** pitch equilibrium of the wings ψ_0, **d** stiffness of the joints k_{rot}, **e** pitch angle of the body θ_{pitch}, **f** stroke bias angle of the wings β and **g** overall energy consumption E_{TI}

7.2 Method Comparison: Performance and Energy Consumption

Several simulated trajectory tracking experiments are chosen to be repeated with both controllers of Section 6. Some of these results are presented here to compare flight performance and power requirements. To estimate stroke power in both sets of experiments, stroke torque of each wing is calculated first:

$$\tau_{\text{stroke}} = F_D r_{\text{CoP}} + b_\phi \dot{\phi} + J_{\dot{\phi}} \dot{\phi} \tag{37}$$

Here, $b_\phi = 1 \times 10^{-5}$ N·m·s is the passive damping coefficient of each wing when rotating around its stroke axis while J_ϕ represents the wing's moment of inertia along this axis. The calculated value for this parameter is equal to 4.894×10^{-7} N·m·s^2 (Fig. 5 with wing mass $= 2 \times 10^{-4}$ kg).

The energy required for both wings to follow a specific stroke profile, i.e. E_{stroke} is then estimated by:

$$E_{\text{stroke}} = 2 \int_0^t \left| \tau_{\text{stroke}} \dot{\phi} \right| d\hat{t} \tag{38}$$

Since actuation in the second control approach is only limited to changes in stroke profile, Eq. 38 is in fact an estimate of this method's overall energy consumption. As for controller 1, changes in mechanical impedance properties require extra

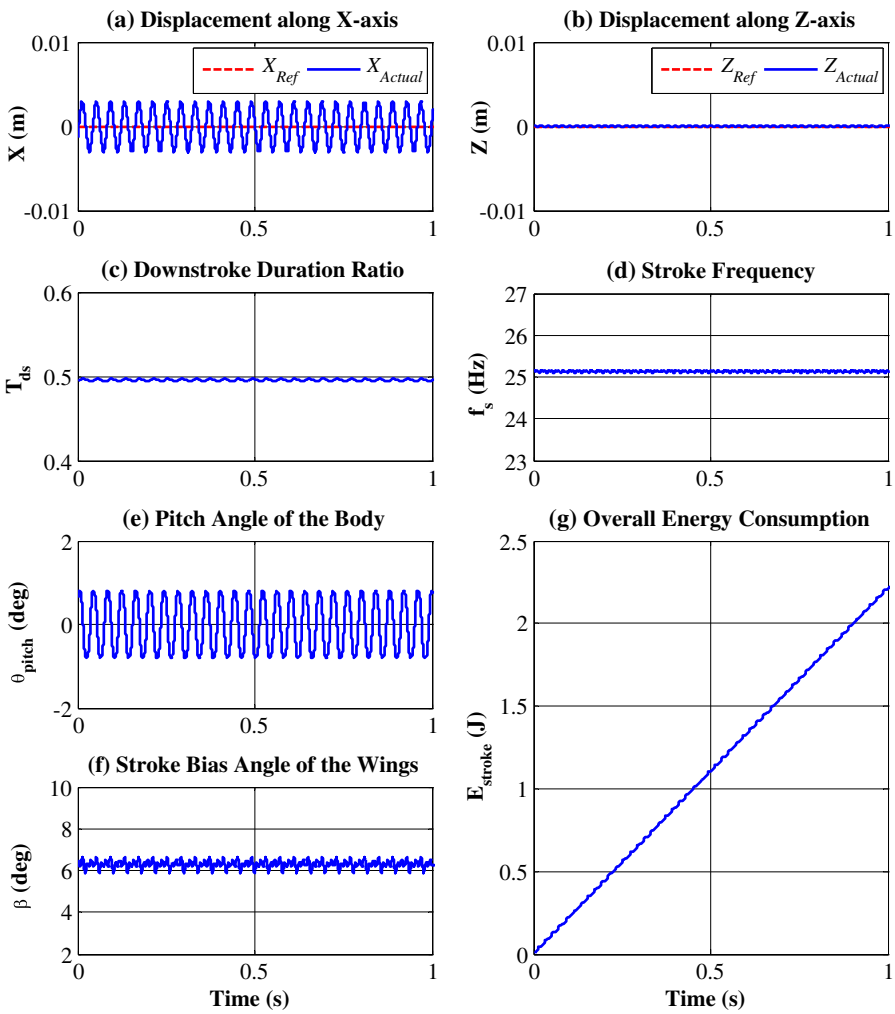

Fig. 20 Simulated results for hovering with controller 2: **a** displacement along X and **b** Z axes, **c** downstroke duration ratio T_{ds}, **d** stroke frequency f_s, **e** pitch angle of the body θ_{pitch}, **f** stroke bias angle of the wings β and **g** overall energy consumption E_{stroke}

power. Using Eq. 12, total energy consumption in this approach, i.e. E_{TI} is estimated by:

$$E_{\mathrm{TI}} = E_{\mathrm{stroke}} + 2\int_0^t |P_{\mathrm{TI}}|d\hat{t} \tag{39}$$

Based on dimensions of a medium-sized hummingbird, parameters A and R in Eq. 12 are set to appropriate values such that $A^2R^6 = 2.5 \times 10^{-5}\ \mathrm{N^2{\cdot}m^2}$.

7.2.1 Hovering

Perhaps, hovering is the only flight capability that is unique to insects and hummingbirds. Flapping-wing MAVs with a similar stroke pattern are also capable of hovering. In this part, hovering of the MAV model over a period of 1 s has been simulated. The results for controllers 1 and 2 are plotted in Figs. 19 and 20, respectively.

From these diagrams, it is observed that both controllers are able to achieve stable hovering without requiring significant changes in their output values. Since all control outputs remain close to their nominal values, it can be concluded that: 1) body pitch profiles in both approaches are close and 2) the value of P_{TI} for controller 1 is insignificant. As a result, both cases should have similar power requirements. In fact over a hovering period of 1 s, energy consumption with controllers 1 and 2 is estimated to be 2.2116 J and 2.2078 J, respectively (Figs. 19g and 20g). Energy-time profiles in both cases are approximately

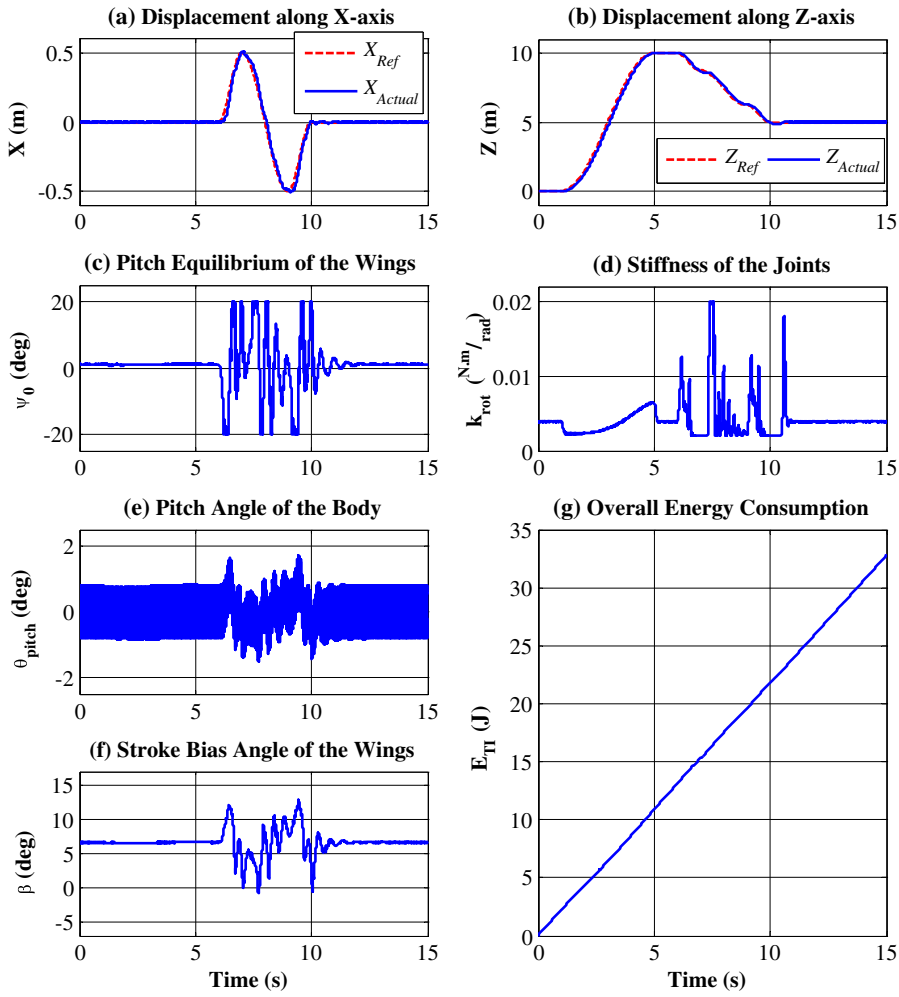

Fig. 21 Simulated results for vertical takeoff and zigzag descent with controller 1: **a** displacement along X and **b** Z axes, **c** pitch equilibrium of the wings ψ_0, **d** stiffness of the joints k_{rot}, **e** pitch angle of the body θ_{pitch}, **f** stroke bias angle of the wings β and **g** overall energy consumption E_{TI}

linear, suggesting a constant energy consumption rate of 2.2116 Watt and 2.2078 Watt, respectively. Note that these values are required to maintain levitation and do not represent cost of transportation.

It is worth mentioning that hummingbirds spend up to 85 % of their time sitting and digesting [38]. The rest is spent for various flight activities that often involve foraging. In [39], it has been observed that a 4.3-gram Broad-tailed hummingbird consumes about 7.31 Calories of sugar per day. If the energy consumed at rest is ignored, this amount would be equivalent to an approximate in-flight energy consumption rate of 2.36 Watt which is close to the power requirements of our MAV model during hovering.

7.2.2 Vertical Takeoff Followed by Zigzag Descent

The results of a takeoff/descent maneuver with controllers 1 and 2 are respectively plotted in Figs. 21 and 22. In these experiments, the hovering model is initially commanded to vertically takeoff such that it reaches an altitude of 10 m within 4 s. After 1 s of hovering at this altitude, the model must descend to a height of 5 m within another 4 s. However, reference displacements along X and Z-axes are designed such that this part of the trajectory follows a zigzag pattern (Figs. 21a, b and 22a, b).

Both employed control strategies are able to precisely navigate the model along this trajectory

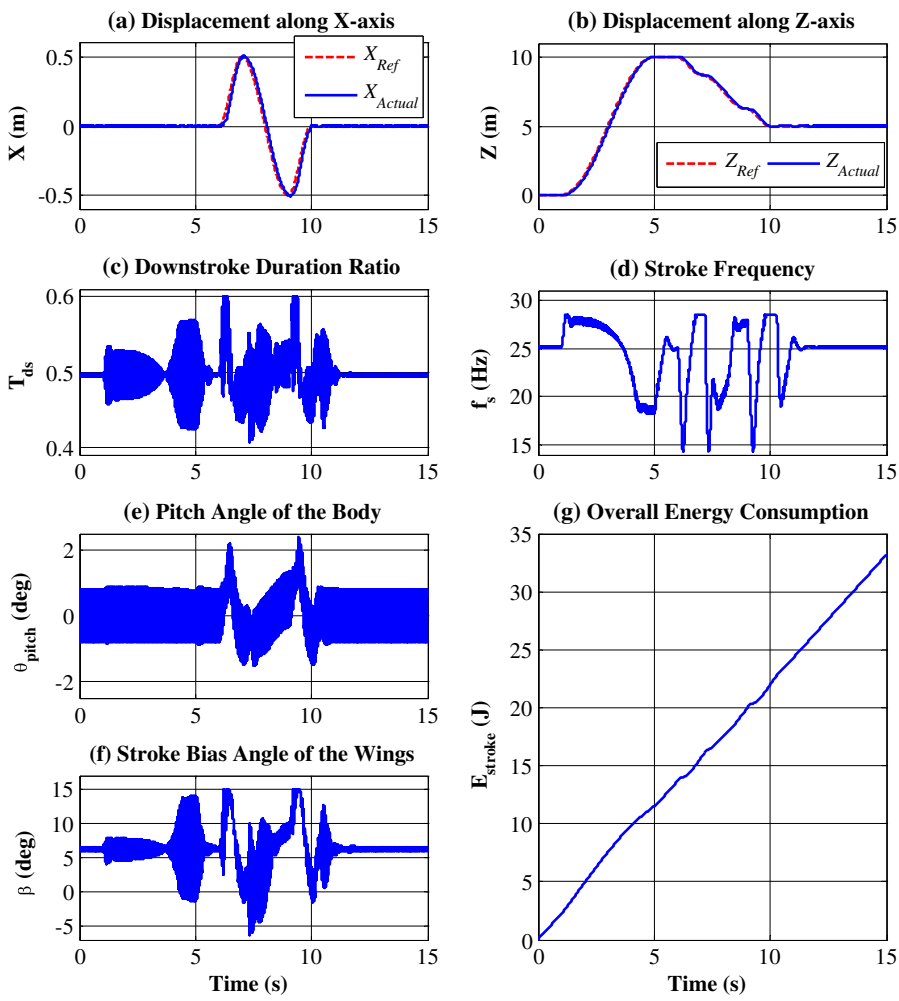

Fig. 22 Simulated results for vertical takeoff and zigzag descent with controller 2: **a** displacement along X and **b** Z axes, **c** downstroke duration ratio T_{ds}, **d** stroke frequency f_s, **e** pitch angle of the body θ_{pitch}, **f** stroke bias angle of the wings β and **g** overall energy consumption E_{stroke}

(Fig. 21a, b and 22a, b). Note that during takeoff with controller 1, the outputs of thrust and pitch sub-controllers are almost constant ($t = 1\,s$ to $t =$ 5 s in Fig. 21c and f). The same is not true for controller 2 (Fig. 22c and f). Furthermore, compared to controller 1, it seems the thrust and pitch sub-controllers in controller 2 have to operate at higher frequencies in order to provide the same overall performance.

Compared to hovering experiments, the model with controller 1 does not demonstrate considerable changes in terms of energy consumption. From Fig. 21g, average power requirements during takeoff and descent maneuvers are estimated as 2.1651 Watt and 2.1596 Watt, respectively. Note that these values are slightly less than power requirements during hovering. From Eq. 12, only a small fraction of overall power (less than 1 %) is spent for impedance manipulation (Fig. 21c, d). The rest, i.e. E_{stroke}, is used to maintain a sinusoidal stroke profile with constant magnitude and frequency. Therefore, from Eqs. 37 and 38, β and F_D are the only variables that can affect average stroke power requirements. Changes in β are often small and slow (Fig. 21f). As for F_D, it has been previously shown [23] that around k_{op}, smaller values of stiffness decrease the magnitude of this force. Hence, the slight reduction in overall value of E_{stroke} (and E_{TI}) in this experiment is primarily due to changes in stiffness (Fig. 21d).

Unlike controller 1, controller 2 relies on modification of stroke properties. Thus, Eqs. 37 and 38 imply that power requirements in experiments with this controller will depend on desired

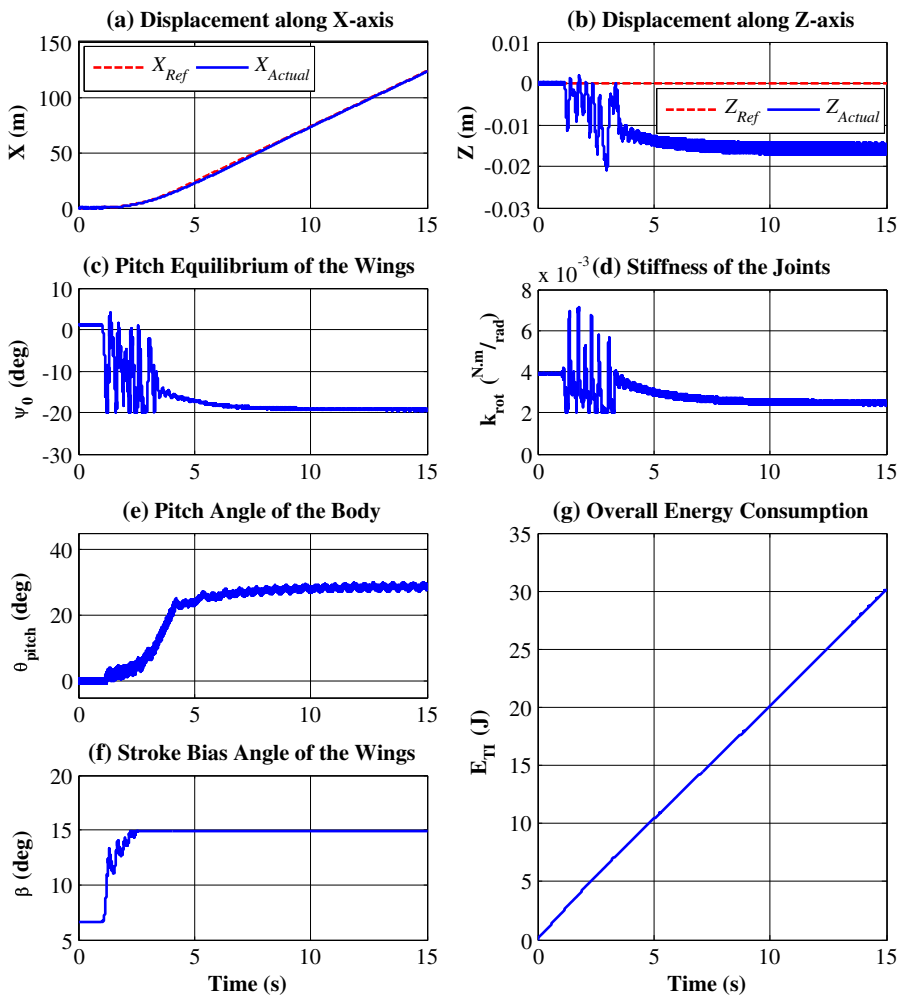

Fig. 23 Simulated results for forward flight at 10 m·s^{-1} with controller 1: **a** displacement along X and **b** Z axes, **c** pitch equilibrium of the wings ψ_0, **d** stiffness of the joints k_{rot}, **e** pitch angle of the body θ_{pitch}, **f** stroke bias angle of the wings β and **g** overall energy consumption E_{TI}

maneuver. From Fig. 22g, these requirements during takeoff and descent maneuvers are estimated as 2.3164 Watt and 2.1876 Watt, respectively. The power used for takeoff is approximately 5 % more than hovering requirements. Since necessary lift for takeoff is achieved through faster stroke cycles (Fig. 22d), the increase in energy consumption is to be expected. As for descent, a similar argument can be used to justify the slight reduction in power requirements compared to those of hovering mode.

7.2.3 Forward Flight at High Velocities

Although average flight speed of hummingbirds is about 5–7 $m{\cdot}s^{-1}$, they are known to be able to reach velocities as high as 14 $m{\cdot}s^{-1}$ [40]. The thrust boost necessary for such velocities is provided through forward pitching of the body. The downside to this strategy is that it also reduces the maximum possible value of lift; hence, vertical maneuvers at such velocities are very challenging.

The presented flapping-wing MAV model also demonstrates such behavior with both controller 1 and 2. Here, the model can reach velocities as high as 10 $m{\cdot}s^{-1}$ before lift sub-controllers fail to stabilize its altitude. The simulated results with controller 1 and 2 at 10 $m{\cdot}s^{-1}$ are illustrated in Figs. 23 and 24, respectively. In both cases, the strained performance of lift sub-controller results in a slight altitude loss (Figs. 23b and 24b).

From Fig. 23g, the model with controller 1 requires only 2.0018 Watt to maintain its target velocity. This value is 9.5 % lower than the power

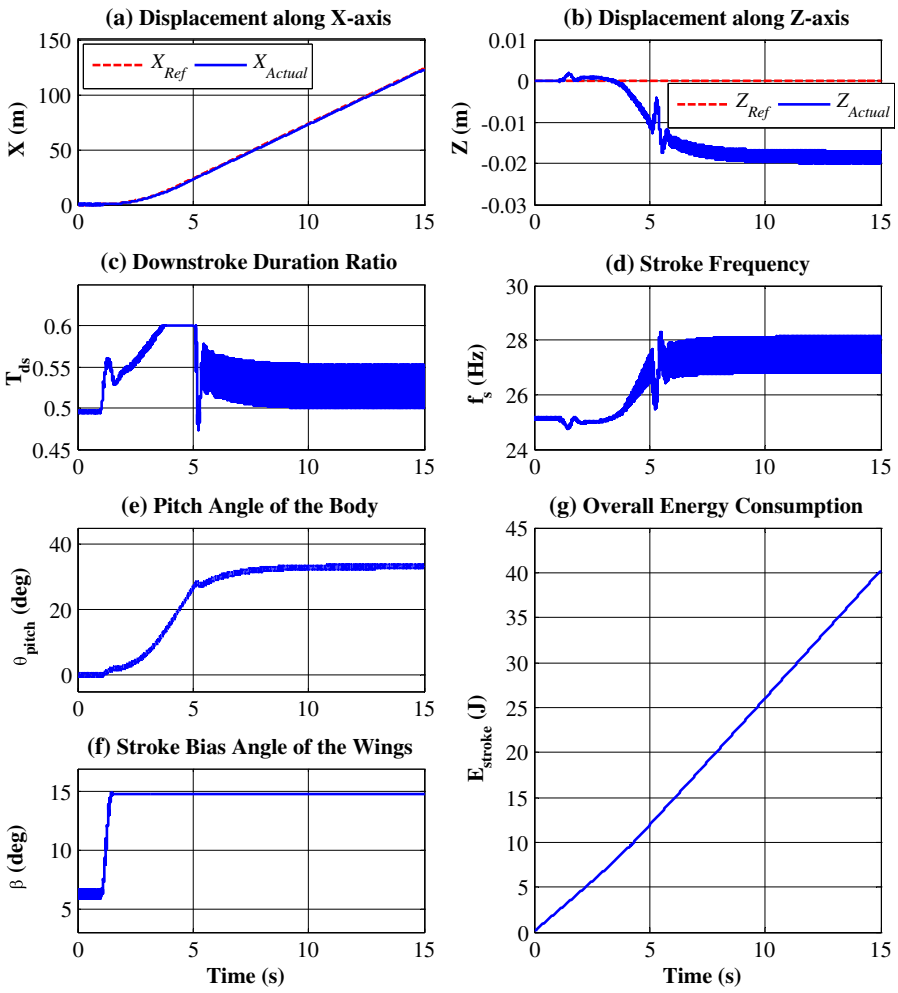

Fig. 24 Simulated results for forward flight at 10 $m{\cdot}s^{-1}$ with controller 2: **a** displacement along X and **b** Z axes, **c** downstroke duration ratio T_{ds}, **d** stroke frequency f_s, **e** pitch angle of the body θ_{pitch}, **f** stroke bias angle of the wings β and **g** overall energy consumption E_{stroke}

required for hovering. Similar to the takeoff experiment in Section 7.2.2, this reduction is caused by lowered values of stiffness (Fig. 23d).

The model with controller 2 reaches target velocity through employing higher values of stroke frequency (Fig. 24d). From Fig. 24g, this approach requires 2.8541 Watt which is 29.3 % larger than the power required for hovering. Note that for the same maneuver with controller 1, required power is reduced by 0.8523 Watt, i.e. almost 30 %.

8 Conclusions

Inspired by insect/hummingbird flight, tunable impedance has been proposed as a semi-passive approach to force manipulation in flapping-wing MAVs. This method states that pitch rotation profile of each wing can be modified through changes in mechanical impedance properties of its joint (Fig. 6). Consequently, as shown by Eq. 25, magnitude of variations and average value of this profile are influential factors in adjustment of aerodynamic forces. Therefore, regulation of mechanical impedance properties can be used as an indirect means of controlling these forces (Fig. 7).

The primary advantage of TI over conventional methods of force control is that it requires no modification in stroke profile of either wing. In fact, both wings can use the same sinusoidal pattern of flapping with fixed parameters – except for stroke bias angle β which is an independent control parameter. This effectively simplifies the control system and can reduce the amount of onboard hardware in an actual prototype. Under this approach, the system is also more controllable and has a higher degree of mobility [26]. However, lift and thrust control are not completely decoupled which at times may result in limited maneuverability of the vehicle.

In this work, we showed that in a system with TI as its underlying strategy for force control, coupling between lift and thrust effectively occurs when either impedance variable carries significant components at high frequencies, i.e. close to the wing-beat rate (Fig. 12). Removing high frequency content from both impedance parameters will considerably reduce lift/thrust coupling and results in better performance compared to our previous work [26]. In fact, a simple control structure such as Fig. 14 is sufficient to stabilize motion along various trajectories.

Results of simulated experiments in Section 7 verify the tracking capabilities of this method. It has been observed that as long as a trajectory can be described using smooth velocity profiles, the only concern for successful tracking is the corresponding acceleration requirements. While imposed limits on impedance parameters guarantee linear relationships with forces, they also restrict acceleration capabilities of the model (Fig. 7). Thus, successful tracking also requires that time-derivatives of these velocity profiles lie within acceleration limits of the model. In a real system, designing such profiles relies on information from both environment and vehicle itself. A high level controller must first come up with an appropriate trajectory based on surroundings of the vehicle and relative location of its target. The current velocity and acceleration limits of the MAV must then be treated as constraints of designing a suitable velocity profile for tracking purposes.

The second goal of this work was to investigate the impact of Tunable Impedance approach on power requirements of a flapping-wing MAV. It was observed that the necessary amount of energy for impedance manipulation is a lot smaller than the amount required for stroke motion. Since stroke profile is approximately constant, the total power requirement in this approach is almost independent of desired maneuver. For the simulated MAV model in this paper, the required power is always less than 2.21 Watt. Interestingly, this value is in agreement with average in-flight energy consumption rate of a hummingbird with similar body dimensions.

In comparison to Tunable Impedance, other control approaches that rely on manipulation of stroke properties often require considerably greater amounts of power. This increase in power consumption is specifically observed when a maneuver demands more lift or thrust production (e.g. forward acceleration in Fig. 24). Faster stroke motions are usually employed to provide for this excess in force requirements.

The gap in energy consumption will widen further when we consider the case in which pitch rotation of the wing is not governed by a passive

mechanism. Consequently, additional actuators are required to directly rotate the wing and modify its angle of attack throughout each stroke cycle. From Eqs. 14 and 24, one can estimate the active torque $\tau_\psi = \tau_{\text{ext}}$ that must be applied to each wing so that it follows a predefined pitch profile ψ. The energy required for active pitch rotation of both wings, i.e. E_ψ is then calculated as:

$$E_\psi = 2\int_0^t \left|\tau_\psi \dot{\psi}\right| d\hat{t} \tag{40}$$

From Eq. 40, if the model with controller 2 were to actively generate the same wing pitch profiles as the simulations in Section 7.2, its power requirements would increase by 0.5571 Watt during hovering, 0.6613 Watt during takeoff and 0.9540 Watt when moving forward at 10 $\text{m}\cdot\text{s}^{-1}$.

As a bio-inspired control strategy with low power demands, the Tunable Impedance method is a promising solution to both problems of maneuverability and power efficiency in flapping-wing MAVs. Considering the limitations of available batteries, implementation of this approach may significantly improve flight time. Our future work is focused on development of appropriate actuators for impedance manipulation. Above all, such actuators must have minimized loading effects so that wing's dynamics are not greatly perturbed. Upon achieving satisfactory results in impedance manipulation, our eventual goal is to install the designed actuators on a 3-inch-wingspan flapping-wing MAV and conduct actual flight experiments.

References

1. Cook, K.L.B.: The silent force multiplier: the history and role of UAVs in warfare. In: 2007 IEEE Aerospace Conf., Big Sky, MT, USA, 3–10 March 2007
2. Osborne, M.F.M.: Aerodynamics of flapping flight with application to insects. J. Exp. Biol. **28**(2), 221–245 (1951)
3. Ellington, C.P.: The aerodynamic of hovering insect flight I. The quasi-steady analysis. Philos. Trans. R. Soc. Lond. B Biol. Sci. **305**(1122), 1–15 (1984)
4. Dickinson, M.H., Lehmann, F., Sane, S.P.: Wing rotation and the aerodynamic basis of insect flight. Science **284**(5422), 1954–1960 (1999)
5. Floreano, D., Zufferey, J.C., Srinivasa, M.V., Ellington, C.P.: Flying Insects and Robots, Springer (2010)
6. Cheng, B., Deng, X.: Near-hover dynamics and altitude stabilization of an insect model. In: 2010 American Control Conf. (ACC), Baltimore, MD, USA, 30 June–2 July 2010
7. Sane, S.P.: Steady or unsteady? Uncovering the aerodynamic mechanisms of insect flight. J. Exp. Biol. **214**, 349–351 (2011)
8. Whitney, J.P.: Design and Performance of Insect-Scale Flapping-Wing Vehicles (PhD Dissertation). Harvard University, USA (2012)
9. Wood, R.J.: The first takeoff of a biologically inspired at-scale robotic insect. IEEE Trans. Robot. **24**, 341–347 (2008)
10. de Croon, G.C.H.E., de Clerq, K.M.E., Ruijsink, R., Remes, B., de Wagter, C.: Design, aerodynamics, and vision-based control of the DelFly. Int. J. Micro Air Vehicles. **1**(2), 71–97 (2009)
11. Michelson, R., Helmick, D., Reece, S., Amarena, C.: A reciprocating chemical muscle (RCM) for micro air vehicle 'Entomopter' flight. In: The Association for Unmanned Vehicle Systems International (AUVSI), Baltimore, MD, USA, 3–6 June 1997
12. Hsiao, F.Y., Chen, C.L., Shen, J.F.: Altitude control of flapping-wing MAV using vision-based navigation. In: 2010 American Control Conf. (ACC), Baltimore, MD, USA, 30 June–2 July 2010
13. Perez-Arancibia, N.O., Barrows, G.L., Wood, R.J.: Altitude feedback control of a flapping-wing microrobot using an on-board biologically inspired optical flow sensor. In: 2012 IEEE Int. Conf. Robotics and Automation (ICRA), St Paul, MN, USA, 14–18 May 2012
14. Malhan, R., Benedict, M., Chopra, I.: Experimental studies to understand the hover and forward flight performance of a MAV-scale flapping wing concept. J. Am. Helicopter Soc. **57**, 1–11 (2012)
15. Doman, D.B., Oppenheimer, M.W., Sigthorsson, D.O.: Wingbeat shape modulation for flapping-wing micro-air-vehicle control during hover. J. Guid. Control Dyn. **33**(3), 724–739 (2010)
16. Jones, E., Vachtsevanos, G.: Fixed frequency, variable amplitude (FiFVA) actuation systems for micro aerial vehicles. In: 2011 IEEE Int. Conf. Robotics and Automation (ICRA), Shanghai, China, 9–13 May 2011
17. Perez-Arancibia, N.O., Whitney, J.P., Wood, R.J.: Lift force control of flapping-wing microrobots using adaptive feedforward schemes. IEEE Trans. Mechatron. **18**(1), 155–168 (2013)
18. Doman, D.B., Oppenheimer, M.W.: Dynamics and control of a minimally actuated biomimetic vehicle: part II. Control. In: AIAA Guidance, Navigation, and Control Conf. Chicago, IL, USA, 10–13 August 2009
19. Deng, X., Schenato, L., Wu, W.C., Sastry, S.S.: Flapping flight for biomimetic robotic insects: part I–system modeling. IEEE Trans. Robot. **22**(4), 776–788 (2006)
20. Mahjoubi, H., Byl, K.: Tunable impedance: a semi-passive approach to practical motion control of insect-inspired MAVs. In: 2012 IEEE Int. Conf. Robotics and Automation (ICRA), St Paul, MN, USA, 14–18 May 2012

21. Dudley, R.: The Biomechanics of Insect Flight: Form, Function, Evolution. Princeton University Press, USA (2000)
22. Mahjoubi, H., Byl, K.: Insect flight muscles: inspirations for motion control in flapping-wing MAVs. In: 2012 Int. Conf. Unmanned Aircraft Systems (ICUAS), Philadelphia, PA, USA, 12–15 June 2012
23. Mahjoubi, H., Byl, K.: Modeling synchronous muscle function in insect flight: a bio-inspired approach to force control in flapping-wing MAVs. J. Int. Robot. Syst. **70**(1–4), 181–202 (2013)
24. Bergou, A.J., Xu, S., Wang, Z.J.: Passive wing pitch reversal in insect flight. J. Fluid Mech. **591**, 321–337 (2007)
25. Mahjoubi, H., Byl, K.: Analysis of a tunable impedance method for practical control of insect-inspired flapping-wing MAVs. In: 2011 IEEE Conf. on Decision and Control and European Control Conference (CDC-ECC), Orlando, FL, USA, 12–15 December 2011
26. Mahjoubi, H., Byl, K.: Steering and horizontal motion control in insect-inspired flapping-wing MAVs: the tunable impedance approach. In: 2012 American Control Conf. (ACC), Montreal, QC, Canada, 27–29 June 2012
27. Unknown Author: Insect Wings. Amateur Entomologists' Society Webpage. http://www.amentsoc.org/insects/fact-files/wings.html (2013). Accessed 27 Sept 2013
28. Schultz, A.B., Faulkner, J.A., Kadhiresan, V.A.: A simple hill element-nonlinear spring model of muscle contraction biomechanics. J. Appl. Physiol. **70**(2), 803–812 (1991)
29. Dickinson, M.H.: The effects of wing rotation on unsteady aerodynamic performance at low Reynolds numbers. J. Exp. Biol. **192**, 179–206 (1994)
30. Willmott, A., Ellington, C., van den Berg, C., Thomas, A.: Flow visualization and unsteady aerodynamics in the flight of the hawkmoth Manduca sexta. Philos. Trans. R. Soc. Lond. B Biol. Sci. **352**, 303–316 (1997)
31. Sane, S.P.: The aerodynamics of insect flight. J. Exp. Biol. **206**, 4191–4208 (2003)
32. Fung, Y.C.: An Introduction to the Theory of Aeroelasticity. Dover Publications, Inc. NY, USA (1969)
33. Sane, S.P., Dickinson, M.H.: The control of flight by a flapping wing: lift and drag production. J. Exp. Biol. **204**, 2607–2626 (2001)
34. Dickson, W.B., Dickinson, M.H.: The effect of advance ratio on the aerodynamics of revolving wings. J. Exp. Biol. **204**(207), 4269–4281 (2004)
35. McKelvey, T., Akcay, H., Ljung, L.: Subspace-based multivariable system identification from frequency response data. IEEE Trans. Autom. Control. **41**(7), 960–979 (1996)
36. Hedrick, T.L., Cheng, B., Deng, X.: Wingbeat time and the scaling of passive rotational damping in flapping flight. Science **324**(5924), 252–255 (2009)
37. Mahjoubi, H., Byl, K.: Trajectory tracking in sagittal plane: decoupled lift/thrust control via tunable impedance approach in flapping-wing MAVs. In: 2013 American Control Conf. (ACC), Washington, DC, USA, 17–19 June 2013
38. Wolf, L.L., Hainsworth, F.R.: Time and energy budgets of territorial hummingbirds. Ecol. **52**(6), 980–988 (1971)
39. Pearson, O.P.: The daily energy requirements of a wild Anna hummingbird. The Condor **56**(6), 317–322 (1954)
40. Gill, F.B.: Hummingbird flight speeds. The Auk **102**(1), 97–101 (1985)